processes

MDPI

Article

Integration of Process Modeling, Design, and Optimization with an Experimental Study of a Solar-Driven Humidification and Dehumidification Desalination System

Mohammed Alghamdi [1,*], Faissal Abdel-Hady [1], A. K. Mazher [2] and Abdulrahim Alzahrani [1]

[1] Chemical and Materials Engineering Department, King Abdulaziz University, Jeddah 21589, Saudi Arabia; faissalhady@gmail.com (F.A.-H.); azahrani@kau.edu.sa (A.A.)

[2] Nuclear Engineering Department, King Abdulaziz University, Jeddah 21589, Saudi Arabia; amazher@hotmail.com

* Correspondence: mohammed_moghram@hotmail.com; Tel.: +966-50-496-5899

Received: 23 July 2018; Accepted: 5 September 2018; Published: 7 September 2018

Abstract: Solar energy is becoming a promising source of heat and power for electrical generation and desalination plants. In this work, an integrated study of modeling, optimization, and experimental work is undertaken for a parabolic trough concentrator combined with a humidification and dehumidification desalination unit. The objective is to study the design performance and economic feasibility of a solar-driven desalination system. The design involves the circulation of a closed loop of synthetic blend motor oil in the concentrators and the desalination unit heat input section. The air circulation in the humidification and dehumidification unit operates in a closed loop, where the circulating water runs during the daytime and requires only makeup feed water to maintain the humidifier water level. Energy losses are reduced by minimizing the waste of treated streams. The process is environmentally friendly, since no significant chemical treatment is required. Design, construction, and operation are performed, and the system is analyzed at different circulating oil and air flow rates to obtain the optimum operating conditions. A case study in Saudi Arabia is carried out. The study reveals unit capability of producing 24.31 kg/day at a circulating air rate of 0.0631 kg/s and oil circulation rate of 0.0983 kg/s. The tradeoff between productivity, gain output ratio, and production cost revealed a unit cost of 12.54 US$/m^3. The impact of the circulating water temperature has been tracked and shown to positively influence the process productivity. At a high productivity rate, the humidifier efficiency was found to be 69.1%, and the thermal efficiency was determined to be 82.94%. The efficiency of the parabolic trough collectors improved with the closed loop oil circulation, and the highest performance was achieved from noon until 14:00 p.m.

Keywords: desalination; humidification; dehumidification; design; experimental

1. Introduction

The vast majority of the water on Earth is salt water and surrounds available lands. The natural freshwater resources are limited, especially over a stressed water area in the Arabian Peninsula, where renewable energy sources, such as solar energy, are in the highest range. The most common desalination techniques are of a commercial size and designed for large cities, and small populations in villages experience a lack of freshwater availability [1]. Saudi Arabia is located in the Middle East, which has various energy sources, including oil, natural gas, wind and solar radiation [2]. The country is considered one of the largest oil producers in the world, and this industry requires further investment for environmental control in order to reduce the emissions, which contribute to the global warming

issue. Therefore, renewable energy sources are more favorable research topics for the promotion of investment in clean technologies, and solar energy is a promising field of research in this connection. The average annual horizontal irradiation in the country is 2200 kwh/m^2/year (251.14 W/m^2) [2,3], which is in the high range compared to different locations around the world. Saudi Arabia's future expectation of solar power demand would be about 30% by the year 2032 [4]. The average annual horizontal irradiance in Saudi Arabia is shown in Figure 1.

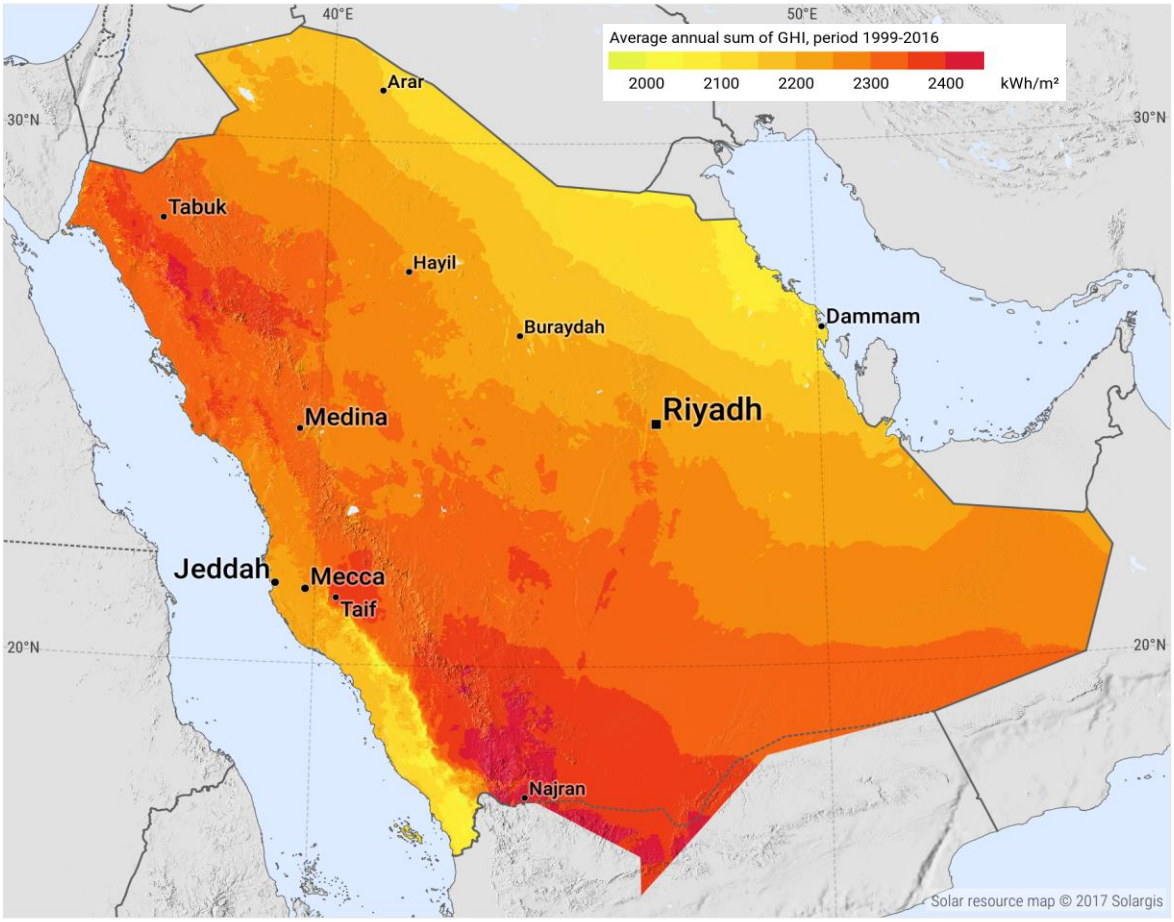

Figure 1. Average annual horizontal irradiation in Saudi Arabia. Reproduced with permission from the solar resource map © 2018 Solargis [5].

Solar energy can be collected using parabolic trough collectors (PTC), which have an efficiency of over 75% [6]. The designed system in this work uses a type SAE 10W-30 synthetic blend engine oil, which circulates through the PTCs to transport the thermal energy to the humidifier heat exchanger; hence, oil flow rates are tested for system performance analysis. The PTCs show higher efficiencies when the circulating fluid rate is increased [7] up to an optimum value, at which a further increase can reduce the efficiency. The flow variation inside the absorber tube is performed [8] in order to relate the Reynolds number to the flow pattern, and the results were obtained in March, April, and May, with a laminar flow. In a review study [9], the PTC performance was found to be dependent on the optical efficiency, circulating fluid heat transfer coefficient, heat flux, reflectance of the reflector, the absorptance, the diameter of the absorber and the length of the collector. The PTC has been used in the desalination field due to its superior performance in solar light tracking and focal receiving [10]. The parabolic concentrator tracking system is used [11] with the tubular solar still for the purpose of desalination, and the resultant production capacities are 0.28, 0.214 and 1.66 L/day, with a production cost of 0.033, 0.044 and 0.024 US$/L, respectively. Moreover, variable pressure humidification and dehumidification (HDH) is used in solar heat in different configurations [12], and the resultant

operating costs were 0.034 and 0.041 US$/L, respectively. The PTC is usually installed where the tracking system is accommodated to enhance the performance of the collector. In a study of PTC, with and without a tracking system coupled with a double slope solar still, the tracking PTC is shown to have a higher still temperature and productivity compared with a non-tracked PTC and conventional solar still [13]. The solar PTC performance varies with different latitude angles in different seasons; hence, the desalination performance shows an increase during the day [14]. A solar driven desalination process can be implemented in arid areas, where large commercial technologies are not economically feasible for a small population; hence, the humidification and dehumidification process can be implemented for this purpose. The sophisticated commercial plants are inadequate in arid areas due to the infrastructure requirements, such as sophisticated switchgears, a power grid, fue transportation and pipelines for small production quantities. Moreover, they require a large number of employees, high technical level and maintenance programs; therefore, the solar HDH becomes a promising process for providing freshwater in arid areas with fewer complications associated with serving a small population village. The HDH process operates at lower temperatures and pressures compared to other desalination techniques, which is advantageous in solar desalination practice. Various arrangements of HDH processes can be implemented, and several studies have been performed in this field in order to improve the process outcome and economics [15]. The air flow rate and temperature are crucial factors in the process, where heating the air supply can increase the specific humidity by 1.22 times compared to the ambient air [16]. The gained output ratio (GOR) increases with an increasing air to water ratio. This increase can be achieved by changing either air or circulating water flow rates, and it may be effective up to an optimal value, at which a further increase in the air to water ratio can reduce the system GOR [17]. Hamed et al. [18] concluded that the solar HDH desalination was strongly affected by ambient conditions and, therefore, that the system temperature rise positively affected the productivity from noon until 5 p.m., with the maximum productivity of 22 L/day and production cost of 0.0578 US$/L. Other parameters, such as the cooling water flow and temperature can alter the system productivity. Ahmed et al. [19] found that the HDH inlet cooling water temperature increases the unit productivity by 10 to 15 L/h, with a production cost of 0.01 US$/L. The solar HDH desalination could improve by understanding the effects of configuration and flow circulation rates on the optimum operating conditions. Combining the HDH desalination unit with a renewable-energy source is the target for sustainability and a clean development process. Solar desalination using collectors is still expensive compared to fossil fuels and needs an improvement in order to convert the solar energy to electrical or thermal energy [20]. In order to investigate its process efficiency and economic viability, the process should be analyzed separately before hybridization with another energy source, such as the available fossil fuel in Saudi Arabia [21]. Based on a review study by Kabeel et al. [15], further HDH design simulation, to understand the effects of air and water flow rates and optimal conditions, was recommended. The use of series PTCs, using the motor oil as an alternative to thermal fluids, and coupled to closed air with the recirculated water HDH system, is a promising design for the research field. This can enhance the desalination options for decentralized areas.

This project was implemented at King Abdul-Aziz University at Jeddah city to study the effect of various factors in the solar-driven HDH desalination unit using six PTCs in a series configuration. The system comprises multiple circulation loops in the solar heating cycle and the desalination air and water cycles. This study aimed to extend knowledge about solar energy utilization in the field of clean environment technologies and provide headway to overcome the freshwater demand in areas in which natural water resources are scarce.

2. Experimental Setup and Procedure

The experiments were performed at the King Abdul-Aziz university campus in an open area to allow for the required incidence from the sun at sunrise and sunset in order to achieve a better project

analysis and evaluation of its performance. The location latitude is 21 degrees, 30 min north, and the longitude is 39 degrees, 15 min east.

2.1. Experimental Setup

The system is designed to utilize solar energy through multiple circulation procedures. The heat input section circulates the oil through the system of the parabolic concentrator, humidifier, bottom heat exchanger, and the oil expansion tank. The water circulates inside the humidifier in order to maintain maximum water temperature and prevent heat loss, which usually occurs in the open water cycle. On the humidifier-packing surface, the water vapor as well as the latent and sensible heat are transferred to the flowing air using a forced circulation technique, which helps to prevent the loss of air and to increase its temperature and humidity. For such a system, the circulating air mostly operates near the saturation curve and close to the equilibrium condition of air to water, therefore improving the humidifier efficiency. The experimental setup for testing the solar humidification and dehumidification desalination system is illustrated in Figure 2. The parabolic concentrators are used to increase the circulating oil temperature, in which the solar tracking system is used to maximize the beam radiation utilization by increasing the useful heat gain of the concentrators. The oil is driven by a gear oil pump, which provides a proper circulation of oil through the PTCs. Therefore, it delivers the gained energy to the heat exchanger on the bottom of the humidifier to circulate the water heating and allows for the oil thermal expansion in the oil tank. The oil circulation procedure allows the system to build up energy instead of using open circuit designs. The quantity of circulating oil in the tank would provide both stability and possible heat storage, since the circulating oil preserves the heat and requires time to complete the circulation cycle. In order to increase the humidifier inlet water temperature and to deliver the necessary sensible heat to the air and water interface, the water circulates through the packing of the humidifier. The water circulation procedure ensures both the heating and humidifying of air, gaining its energy from the heat exchanger on the bottom of the humidifier. The temperature of the circulating air is increased, and the air contains water vapor to deliver to the dehumidifier. In the dehumidifier, the cooling and condensing of the air and water vapor mixture occurs, and part of the water is extracted from the process as a distillate.

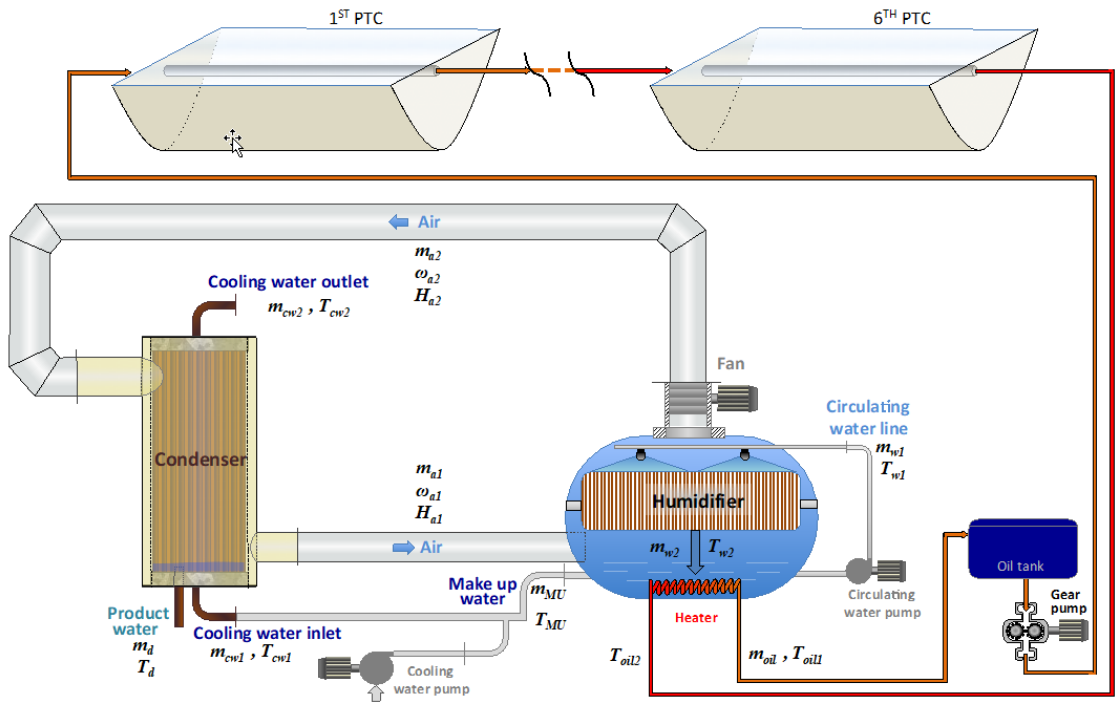

Figure 2. Schematic diagram of the humidifier.

In the dehumidifier the air temperature and its humidity decreased to a point higher than the ambient conditions; therefore, the circulation of this stream allows for further process efficiency improvement. The humidifier circulating water is fed by making water to compensate for the amount of water vapor being transferred to the dehumidifier and is extracted as a process yield. The fabricated and installed major components of the experiment are shown in Figure 3.

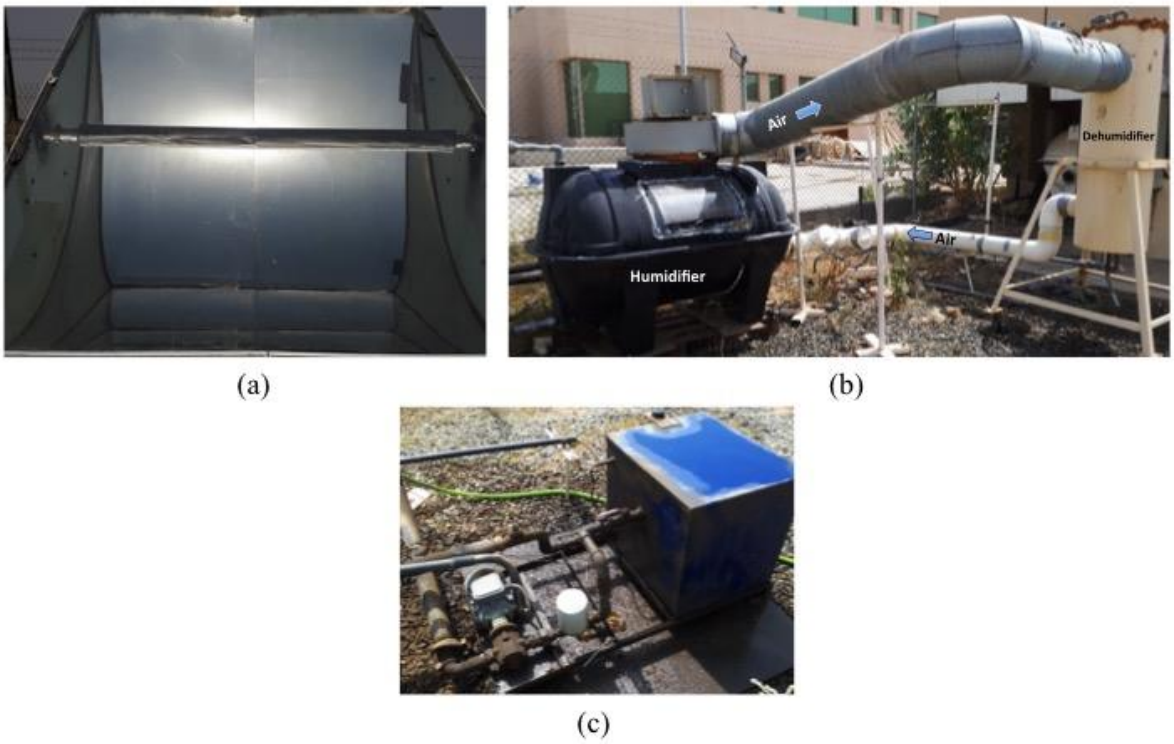

Figure 3. Photos of the experimental setup and main components: (**a**) parabolic trough collector (PTC) with absorber tube; (**b**) humidification and dehumidification (HDH) desalination unit; and (**c**) oil expansion tank.

2.1.1. The Parabolic Concentrators

There are six parabolic concentrators aligned in a series. The solar beam radiation reflects from the concentrator on the lower part of the absorber tube. The six parabolic concentrators are made from glass fiber-reinforced polymer (GFRP), with a thickness of 2.3 mm. The GFRP material was selected due to its availability and cost-effectiveness and, moreover, because it is known to have an excellent thermal insulation. The GFRP are lined with a polymer-based mirror type 3M fused to a stainless steel sheet, with a thickness of 0.5 mm. The polymeric mirror allows the concentrator to have a high efficiency at the working incidence. The dimensions of one PTC used in this experiment are shown in Figure 4. The absorber tube is made from a copper material, which has a high thermal conductivity and is lightweight. The tube is coated with black polymeric paint, which allows the receiver tube to absorb the radiation more efficiently.

The design specification of the PTC and the fabrication material are listed in Table 1. The tracking system of the PTC is designed to work from east to west while the PTCs are oriented in the horizontal north–south direction.

A thermally-treated protective glass covers the aperture plane, which aids in the reduction of the convective thermal loss due to winds flowing around the absorber tube. The solar beam radiation, measured as normal, on the PTC surface during the experiment is recorded by a precise solar power meter. The meter is an instrument, used in the solar research field, of type SM206, with an error range of $\pm 5\%$ of the measured value.

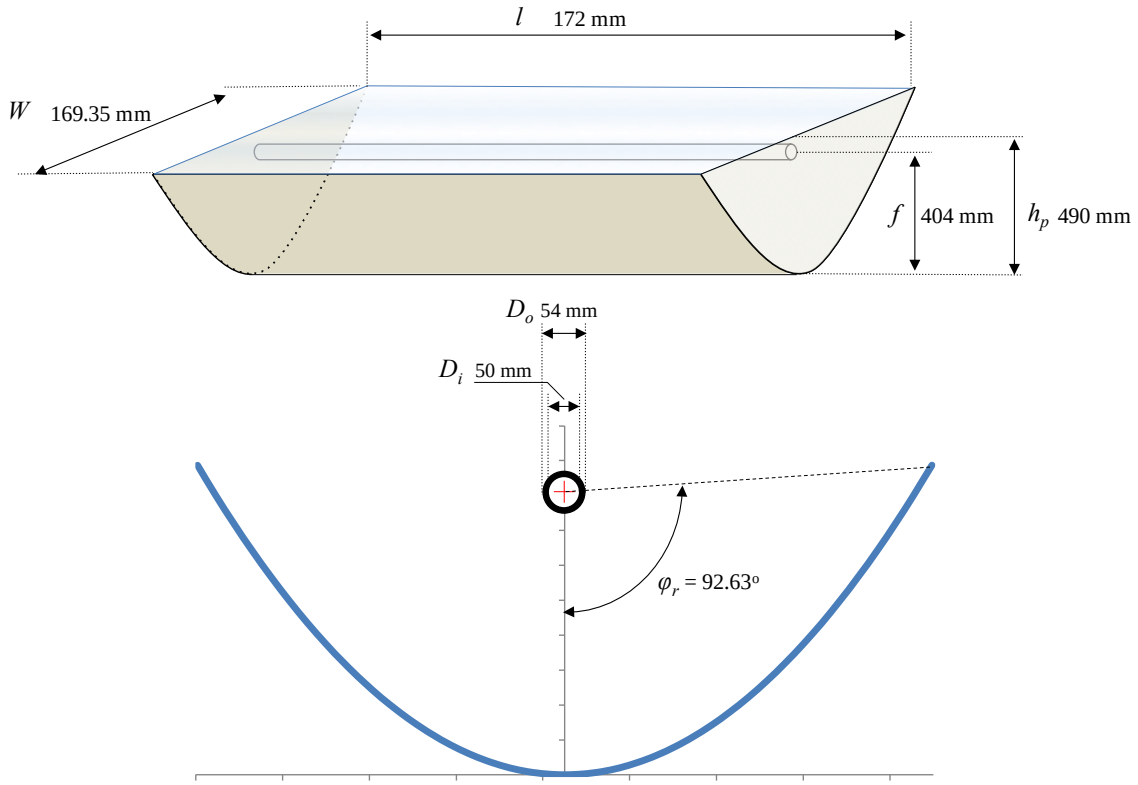

Figure 4. Schematic diagram of the parabolic concentrator.

Table 1. The PTC geometrical parameters.

r_r	Rim radius, m	0.848
φ_r	Rim angle	92.63°
f	Parabola focal distance, m	0.404
D_o	Receiver outside diameter, m	0.054
D_i	Receiver internal diameter, m	0.05
θ_m	Acceptance angle	2.84°
W_a	The aperture width, m	1.694
h_p	Height of the parabola, m	0.49
l	Trough length, m	1.72
C	Geometric concentration ratio	9.89
s	Curve length of the reflective surface, m	1.966
t	Glass thickness, m	0.004
J	Reflector thickness, m	0.001
ξ	Reflectance of the reflector	0.95
τ	Transmittance of the glass cover	0.9
ψ	Absorptance of the receiver.	0.97
γ	Intercept factor	1.000

Engine oil is used as the working fluid in this experiment due to its durability and lower price compared to commercial thermal fluids. The oil type is SAE 10W-30 synthetic blend engine oil. Engine oil has an advantage over water, since oil can sustain higher temperatures unlike water, which evaporates and develops hammering in the pipes, requiring high-quality piping and joint fabrication, and this increases the process capital cost. The thermo-physical properties of the circulating oil can change when its temperature increases during solar heating. The thermo-physical properties, shown in Table 2, are used to proceed with the system calculations.

Table 2. Thermo-physical properties of the SAE 10W-30 synthetic blend engine oil.

T Temp. (K)	ρ Density (kg/m^3)	c_p Specific Heat (kJ/Kg-c)	μ Viscosity (N-s/m^2)	ν Kinematic Viscosity (10^{-4} m^2/s)	k Thermal Conductivity (W/m-K)
260	908	1.76	12.23	135	0.149
280	896	1.83	2.17	24.2	0.146
300	884	1.91	0.486	5.50	0.144
320	872	1.99	0.141	1.62	0.141
340	860	2.08	0.053	0.62	0.139
360	848	2.16	0.025	0.30	0.137
380	836	2.25	0.014	0.17	0.136
400	824	2.34	0.009	0.11	0.134

2.1.2. Humidification and Dehumidification Unit

The humidifier tank is made from fiberglass-reinforced plastic (FRP) material that has the following advantages: it is lightweight, corrosion resistant, cost-effective and robust enough to handle the system working pressure and temperature. There are different sizes available for such a tank, which can be selected upon the operating capacities of the desalination unit. Moreover, the humidifier body is painted with a black polymer coating to enhance the sunbeam radiation absorption during the day, when the temperature of the system, designed to promote the circulating water, increases. The FRP material is known to have a low thermal conductivity; hence, the combination of both FRB and black paint will enhance the energy conservation in the humidifier. The opening on the top of the humidifier is equipped with a forced draft fan, driven by a 220 v 3-phase motor, to circulate the humid air through the system. A schematic diagram of the humidifier components, dimensions, and flow openings is shown in Figure 5. Several ports are fabricated for the returned air flow from the dehumidifier, makeup water line, circulating water inlet and oil circulation through the bottom heater. The humidifier is internally packed with canvas sheets to promote air-to-water contact by increasing the surface area due to its high porosity. This material is selected for its common availability, low cost and easy replacement, which reduces both capital and running costs. The packing material is supported in the middle of the humidifier tank using a transparent acrylic sheet manufactured from a synthetic polymer. The acrylic sheet is also used to seal and prevent air from passing around the packing in a shortcut, away from the packing. It is installed using adhesives around the middle edge of the humidifier, where the packing is placed. The circulating water is introduced into the humidifier through two top nozzles to ensure a conical shape of flow covering the packing surface area. Both nozzles are capable of delivering a circulating water pump capacity of 0.571 kg/s. The circulating air and water are flowing in a counter flow pattern inside the humidifier. The circulating water is a forced type, using a single-phase constant speed pump driven by a 220 v motor. The bottom heater of the humidifier is an unmixed counter flow heat exchanger, typically used in the internal combustion engine cooling system of automobiles. The heat exchanger manufacturing material is aluminum, with a total surface area of 11.074 m^2. The heating oil flows inside the tubes are crosswise to the circulating water direction, where the water is maintained above the heat exchanger using a float valve in the makeup water inlet port.

The dehumidifier is a vertically mounted shell and tube heat exchanger, with one pass and no baffles. The humid air stream is introduced into the dehumidifier from the top and flows downward to the bottom of the heat exchanger, and it is then released from the outlet port and recycled for the humidifier. A schematic diagram of the dehumidifier shell and tube heat exchanger is shown in Figure 6. The design of the implemented heat exchanger uses 50 copper tubes, each with an outer diameter of 28.5 mm. The height of the copper tubes is 1300 mm, which together provide a 5.817 m^2 contact surface area between the humid air and the cooling water. There are two water boxes for the heat exchanger, which are made from galvanized steel, with a height of 50 mm and 470 mm in diameter, providing 0.0174 m^3 of cooling water for both water boxes. The cooling water flows from the bottom water box upward through the copper tubes and is then released from the top outlet pipe to ensure that the tubes are uniformly filled, even at lower water cooling flow rates. The humid air flows

counter-current to the cooling water stream, in which part of the entrained water vapor condenses at the outer surface of the copper tubes and is then diverted to the distillate water port for collection.

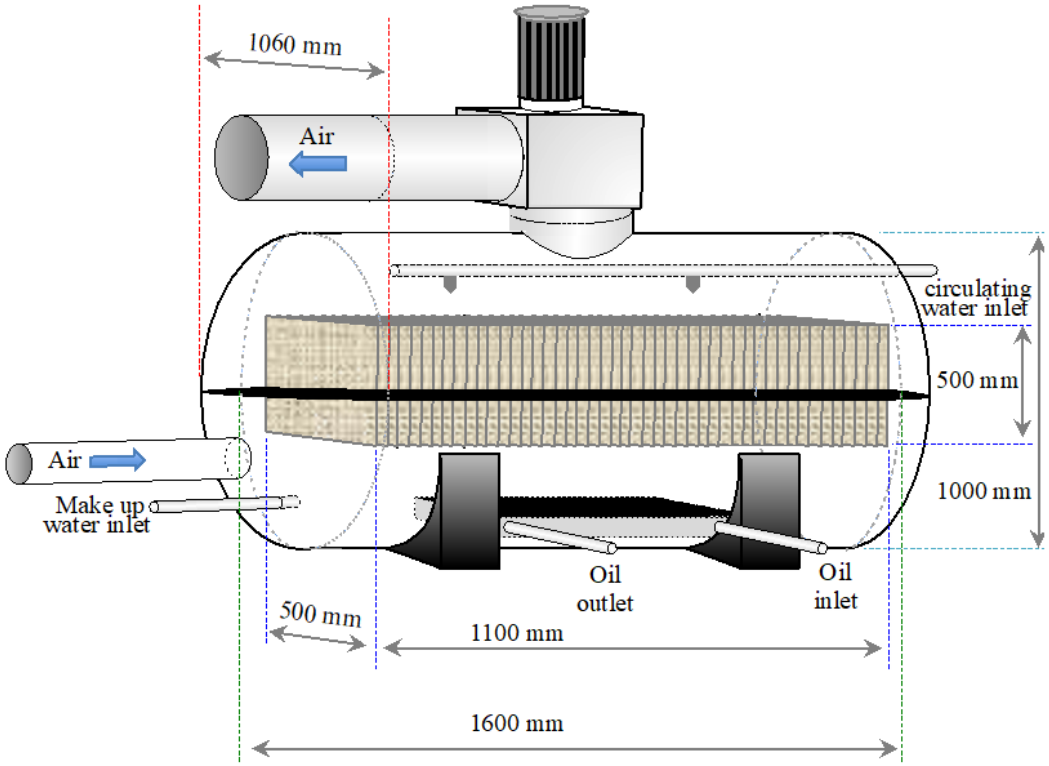

Figure 5. Schematic diagram of the humidifier.

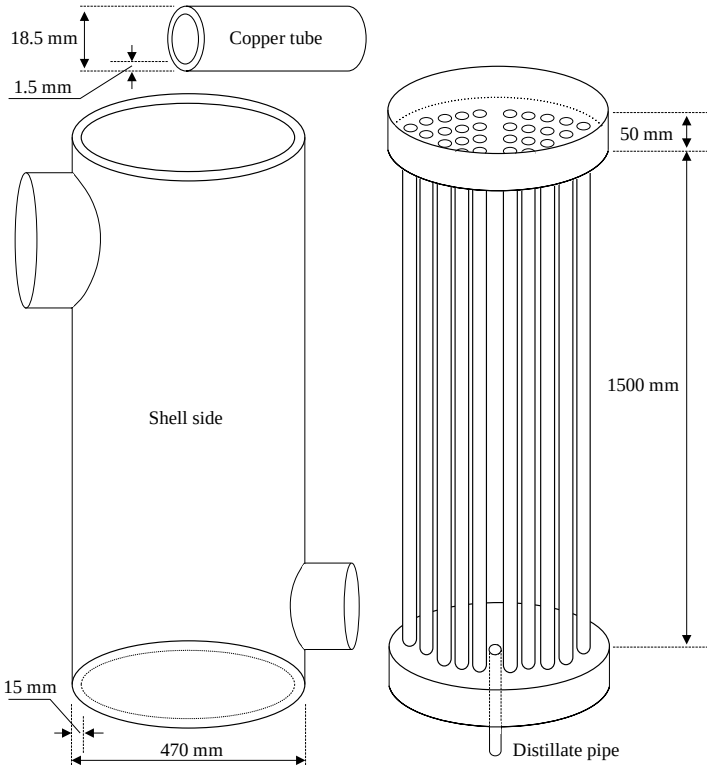

Figure 6. Schematic diagram of the dehumidifier.

2.1.3. Measuring and Controls

Both the desalination unit and the solar tracking system of the PTCs are controlled and monitored using Laboratory Virtual Instrument Engineering Workbench (LabVIEW) software. For solar system tracking, the designed graphical interface using a visual programming language is enabled to control the tracking DC motor motion through the amplified signal, sent by a Galil motion control card. A control loop with a feedback signal allows the motion control system to continuously track throughout the day, as shown in Figure 7.

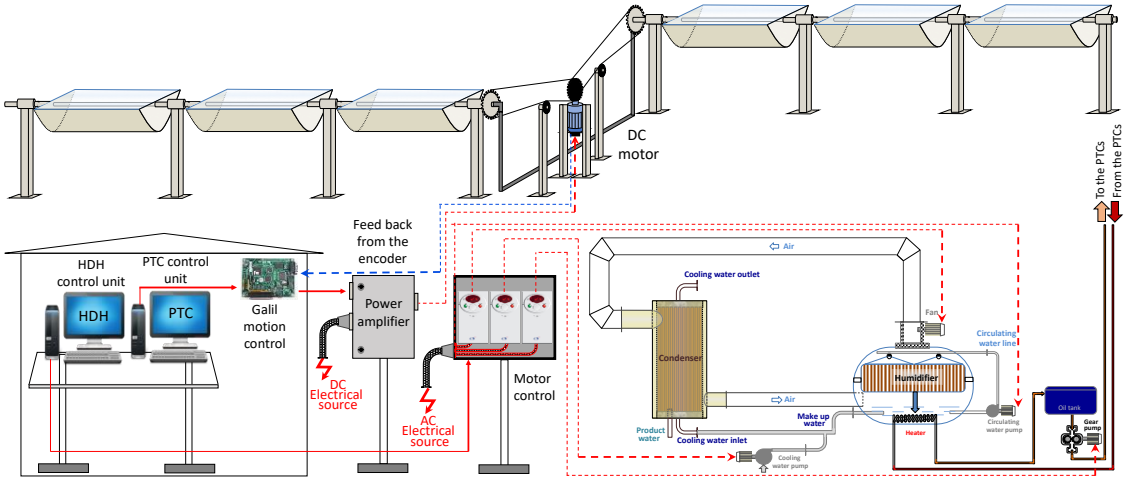

Figure 7. Schematic diagram of the experiment controls.

The east and west rotations of PTCs are protected by limit switches, installed in both directions for controlling the motor operation at sunset, to return the PTCs to the home position and stop the motor when the home position is reached as well as prepare the collector for the sunrise position of the next day. An absolute type encoder, mounted on the DC motor shaft, controls the angular position of the PTCs to monitor the motion activity. The desalination unit drives and the circulating oil pump drive speed are controlled by an AC frequency inverter, which provides a wide range of speed control; hence, the flow capacities are controlled based on the desired testing value. The circulating water pump of the humidifier is kept at a constant speed, while the air circulating fan speed is altered. The system oil/air/water temperatures are measured using K-type thermocouples, which have a wide range of sensing temperatures, with an accepted accuracy at error limits of $\pm 0.75\%$ [22]. The thermocouples are connected to the computer through a field point thermocouple input model. Daytime relative humidity, wind speed, and ambient temperatures are recorded. The circulating air conditions are recorded, and its temperature and humidity are measured by a humidity sensor mounted on the air ducts. The product water from the desalination unit is collected from the distillate port under the dehumidifier and measured in a scaled water storage tank. The measured experimental data uncertainty analysis is described in Appendix A, however, the maximum standard uncertainty is found to be 0.94.

2.2. Experimental Procedure

Each experimental operation and recording is performed on a daily basis. The oil expansion tank level is checked in an adequate position. The oil, air, humidifier water, dehumidifier cooling water circulation are started at 06:20 a.m. daily to ensure the system functionality. The circulation provides a uniform temperature over the cycles and complete humidifier packing constitutes a wet condition. The desired oil and air circulating flow rates are established using the AC frequency inverters. The PTCs are checked in the home position, preparing for the sunrise and tracking the solar motion throughout the day. The computer graphical interface of LabVIEW is initiated to start the

tracking system using a Galil motion control card. Similarly, the system temperatures and humidity recordings are stored in an excel sheet for the whole experiment run. The solar beam radiation is measured as normal on the horizontal level of the PTCs and is recorded every hour. The distillate obtained from the desalination unit is collected and measured hourly. Sun tracking and system recording are continued until the end of the day, when the return limit switch is activated to rotate the PTCs back to the home position. For the next testing conditions, the circulating oil and air flow rates are changed based on the test plan to record several operation modes in order to analyze the designed system performance.

3. Experiment Analysis

The desalination system can be split into three major control volumes in order to perform analyses and calculations for each one. The control volumes are classified as follows:

(1) Solar parabolic concentrator,
(2) Humidifier,
(3) Dehumidifier.

The direction of the heat flow starts from the solar collector through the humidifier to the dehumidifier, where part of the heat is retained by recirculating the air back to the humidifier, and the insignificant heat loss is dumped into the cooling reservoir.

3.1. Parabolic Solar Collector

3.1.1. Solar Irradiance and Tracking Angles

The beam from the sun can generally be considered as the direct beam and diffused beam; hence, the solar irradiance to the parabolic concentrator would be combined beams. Due to the geometrical design of the parabolic concentrator, the direct beam is considered the useful part of the solar irradiance, and it is affected by the incidence angle and called the tilted beam radiation [23], which can be given by the following relation:

$$I = G_{bn} cos(\theta) \quad (1)$$

where I and G_{bn} are the solar irradiance and the normal beam radiation, respectively. The incidence angle θ must be calculated in order to obtain the useful solar irradiance to the parabolic concentrator and can be found by calculating other solar angles.

- Latitude angle (L)

This depends on the location of the site on the Earth and the site of the experiment found above the equator; hence, the latitude of the experiment site is positively valued and found to be 21.5°.

- Hour angle (h)

Solar noon is defined as that time of day when the sun appears due south (north), and the solar time is the time of day measured from solar noon [24]. The reference day hour is 12:00 p.m., where the mid daylight hours are calculated to have the maximum expected radiation. The hour angles are negatively valued for the first half of the day and positively valued in the afternoon. The following relation is employed to calculate the hour angle [17,19]:

$$h = 15^o[t_s - 12] \quad (2)$$

where t_s is the solar time based on the local time and substituted in a 24-h system.

- Declination angle *(δ)*

The declination angel is influenced by the location of the Earth with respect to the sun. The value of this angle varies positively or negatively depending on the season and specifically on the number of days in the year due to the rotation of the Earth. The following relation gives the declination angle [23,25]:

$$\delta = 23.45\left[sin\left(\frac{360}{365}(284+N)\right)\right] \quad (3)$$

where N is the number of the day in the year. For the experiment site, the maximum positive declination angle for the earth is 23.45 in the summer, and the maximum negative value is -23.45 in the winter.

- Altitude angel (α)

The altitude angle is calculated for the horizontal surface of the experiment site. It depends on the elevation of the sun in the sky; hence, the projection of the sunbeam on the horizontal surface forms this angle. Therefore, the experimental site latitude, hour angle and declination angle of the earth with respect to the sun have a great influence on this angle. The following relation is used to calculate it [23,26]:

$$\alpha = sin^{-1}[sin(L)sin(\delta) + cos(L)cos(\delta)cos(h)] \quad (4)$$

- Azimuth angle (ϕ)

The azimuth angle is concerned with the south direction of the experimental site. It is the angle between the south direction of the experimental site and the sunbeam projection on the horizontal site and can be calculated as follows [23]:

$$\phi = sin^{-1}\left[\frac{cos(\delta)sin(h)}{cos(\alpha)}\right] \quad (5)$$

- Surface azimuth angle (ϕ_s)

The surface azimuth angle is the deviation of the projection, on a normal horizontal plane on the surface, from the local meridian [27]. For the present case, where the tracking system operates from east to west, this angle will be either -90°, when the concentrator is facing east, or 90°, when it is facing west [23].

- Zenith angle (θ_z)

The magnitude of the zenith angle is obtained from the difference between the altitude angles and the vertical position on the surface, which depends on the sun's position in the sky. The zenith angle is calculated by the following relation [28]:

$$\theta_z = 90^o - \alpha \quad (6)$$

- The incident angle (θ)

This is the sunbeam projection angle and is measured from the vertical axis to the surface. It is obtained by Kreith and Kreider, and Duffie and Beckman [23,27,29,30], and is shown as follows:

$$\theta = cos^{-1}\left[\sqrt{sin^2(\alpha) + cos^2(\delta)sin^2(h)}\right] \quad (7)$$

3.1.2. Concentrator Thermal Analysis

The optical efficiency of the solar parabolic concentrator is required in order to proceed with the calculation of the thermal efficiency of the system. It represents the percentage of the absorbed solar

irradiance "energy" that falls on the absorber tube. This efficiency accounts for the system's random and non-random errors. The equation used to calculate the optical efficiency is given by [23,27]:

$$\eta_o = \xi\tau\psi\gamma\left[\left(1 - A_f tan(\theta)\right)cos(\theta)\right] \tag{8}$$

where A_f is the geometric ratio between the aperture lost area A_l of the concentrator and the total aperture area A_a and can be obtained by the following relation:

$$A_f = \frac{A_l}{A_a} = \frac{\frac{2}{3}Wh_p + fW\left[1 + \frac{W^2}{48f^2}\right]}{Wl} \tag{9}$$

The geometric ratio of the design parabolic concentrator is calculated and found to be $A_f = 0.511$. The intercept factor γ for the concentrator is obtained by Abdel-Hady F. et al. [31] and found to be 0.84, when the absorber tube outer diameter is 0.42 mm, and still 16.3% of rays dissipated away from the absorber tube. Therefore, the absorber tube diameter is enlarged to 0.54 mm to allow for maximum sunbeam coverage; hence, the intercept factor becomes 1, and the collector concentration ratio $C = W/\pi D_o$ is decreased to 9.984. The lost area, due to the end effect, is not an effective area and is significantly affected by the solar incidence angle θ, which can be calculated by the following relation [23]:

$$A_e = fWtan(\theta)\left[1 + \frac{W^2}{48f^2}\right] \tag{10}$$

The concentrator instantaneous efficiency is known to be the ratio of the amount of heat gained to the amount of solar irradiance that falls on the absorber tube within its effective surface area. The following relation is used to calculate this efficiency [23,27,28]:

$$\eta = \frac{m_{oil}c_{oil}(T_{c-oil-in} - T_{c-oil-out})}{I(A_a - A_e)} \tag{11}$$

The heat removal factor F_R, in Equation (13) is employed to calculate the collector instantaneous efficiency, which is based on the concentrator fluid inlet temperature T_i and ambient temperature [28,30].

$$\eta = F_R\left[\eta_o - \frac{U_L}{C}\left(\frac{T_i - T_a}{I}\right)\right] \tag{12}$$

From the experimental data, obtained daily at different operating conditions, the required variables are measured and analyzed. ASHRAE Standard 93-2003, "Methods of testing to determine the thermal performance of solar collectors" (ASHRAE 2003), is used. The concentrator instantaneous efficiency η is calculated from Equation (12), where the term $(T_i - T_a)/I$ in Equation (13) is measured experimentally. The plot of the instantaneous efficiency against $(T_i - T_a)/I$ reveals the value of $F_R\,\eta_o$, which represents the intercept of the line, and $(F_R U_L/C)$ is the slope of this line; hence, the values of F_R and U_L are obtained. The overall heat transfer coefficient of the absorber tube can be calculated from the following relation [23,28]:

$$U_c = \left[\frac{1}{U_L} + \frac{D_o}{h_{ab}D_i} + \frac{D_o ln\left(\frac{D_o}{D_i}\right)}{2k_{ab}}\right]^{-1} \tag{13}$$

where the convective heat transfer coefficient h_{ab} inside the absorbers tube is calculated from the following relation [32]:

$$Nu = 0.023Re^{0.8}Pr^{0.4} \tag{14}$$

For the fully developed laminar flow pattern, the Nu number value is 4.36 [32]. The Re and Pr numbers are obtained from the following relations, using the fluid properties inside the absorber tube.

$$Re = \frac{4m_{oil}}{\pi D_i \mu_{oil}} \tag{15}$$

$$Pr \frac{c_{oil}\mu_{oil}}{k_{oil}} \tag{16}$$

3.2. Humidifier

3.2.1. Humidifier Bottom Heater Section

A cross flow type heat exchanger, in which the oil flows inside the tubes in a cross direction to the outlet water from the humidifier packing, which flows downward through the heat exchanger, is incorporated in the humidifier. The heat exchanger design parameters and the experimental data are used to calculate the heat exchanger overall heat transfer coefficient in the following manner. The effectiveness relation of the cross-flow heat exchanger, with a single pass and both fluids unmixed, are given below [32,33]:

$$\varepsilon = 1 - exp\left[\left(\frac{1}{C_r}\right)(NTU)^{0.22}\left(exp\left[1 - C_r(NTU)^{0.78}\right] - 1\right)\right] \tag{17}$$

where C_r is the heat capacity ratio, which is given as $C_r = C_{min}/C_{max}$. The heat capacities are calculated for the cold stream $C_w = m_w c_w$, and the hot fluid $C_{oil} = m_{oil}c_{oil}$ is then categorized based on their values as maximum or minimum.

The value of the heat exchanger effectiveness is calculated from the experiment heat analysis as follows:

$$\varepsilon = \frac{q_{HD,in}}{C_{min}(T_{oil,i} - T_{water,i})} \tag{18}$$

From the previously obtained parameters, Equation (18) is solved for the NTU value at the operating condition. Therefore, NTU is used to calculate the overall heat transfer coefficient of the humidifier bottom heat exchanger as shown below.

$$U_{HD} = \frac{(NTU)C_{min}}{A_{HD_{heater}}} \tag{19}$$

The mass and energy balance across the heater is obtained, based on the configuration of the streams, as shown in Figure 7.

Mass balance:

$$m_{w1} = m_{w2} + m_{MU} \tag{20}$$

Energy balance:

$$m_{oil}c_{oil}(T_{oil2} - T_{oil1}) = m_{w2}c_w T_{w2} + m_{MU}c_w T_{MU} - m_{w1}c_w T_{w1} \tag{21}$$

where

$$m_{MU} = m_a(\omega_{a2} - \omega_{a1}) \tag{22}$$

3.2.2. Humidifier Packing Section

According to the designed humidification and dehumidification desalination unit, shown in Figure 8, the heat and mass balance equations are obtained from the control volume 1, as follows:

Mass balance across the packing:

$$m_{w2} - m_{w1} = m_a(\omega_{a2} - \omega_{a1}) \tag{23}$$

Energy balance for air and water streams:

$$m_a(H_{a2} - H_{a1}) = m_{w1}c_w T_{w1} - m_{w2}c_w T_{w2} \tag{24}$$

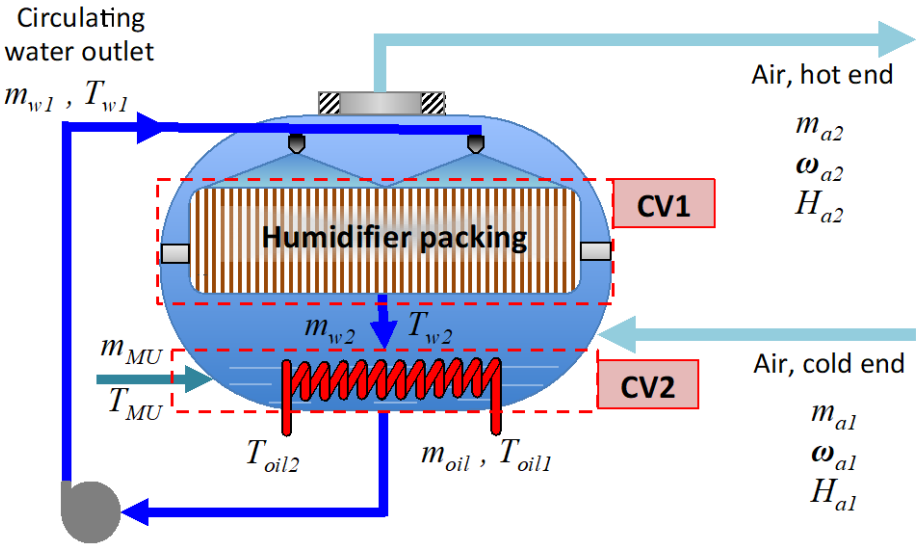

Figure 8. Schematic of the humidifier balance.

The mass transfer coefficient of the humidifier is obtained by using the log mean enthalpy difference (LMED) method. This method showed a good consistency with ε-NTU [34,35]; hence, the formulation of the balance is obtained as follows:

$$m_a(H_{a2} - H_{a1}) = K_y \mathrm{aV} \Delta H_m \tag{25}$$

where ΔH_m is the log mean enthalpy difference:

$$\Delta H_m = \frac{(H_{as2} - H_{a2}) - (H_{as1} - H_{a1})}{ln\left(\frac{(H_{as2} - H_{a2}) - f_c}{(H_{as1} - H_{a1}) - f_c}\right)} \tag{26}$$

where f is the developed analytically-based correction factor, which is calculated from:

$$f_c = \frac{H_{as1} + H_{as2} - 2H_{avg}}{4} \tag{27}$$

3.3. Dehumidifier

The flow streams of the dehumidifier (CV2) are shown in Figure 9. The heat and mass balance of the dehumidifier are formulated as follows:

Mass balance:

$$m_d = m_a(\omega_{a2} - \omega_{a1}) \tag{28}$$

Energy balance:

$$m_a(H_{a2} - H_{a1}) = m_{cw}c_w(T_{cw2} - T_{cw1}) m_d c_w T_d \tag{29}$$

where

$$T_{cw2} = T_d$$

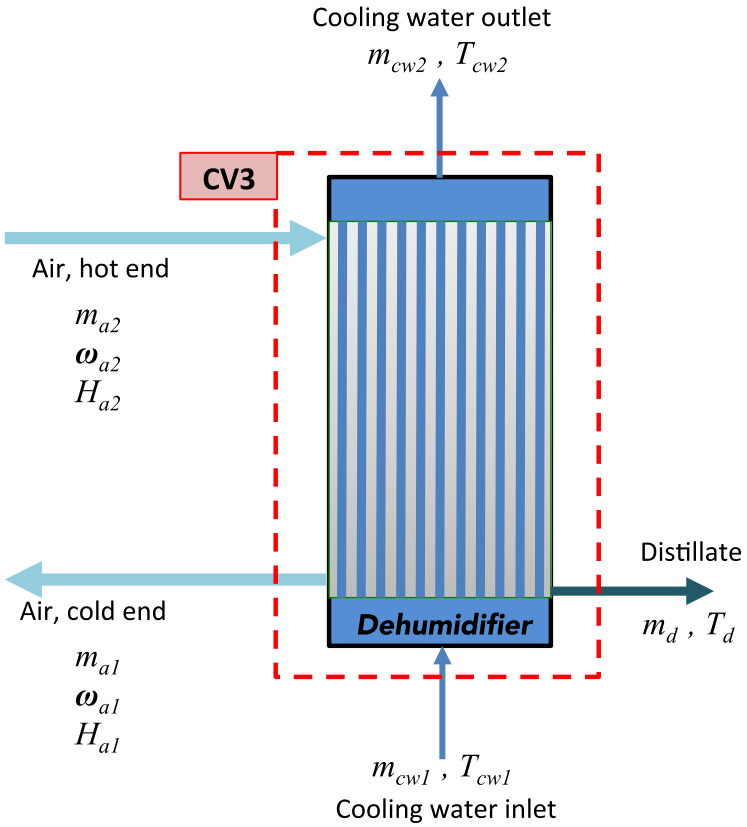

Figure 9. Schematic of the dehumidifier balance.

In order to calculate the overall heat transfer coefficient in the condenser, the log mean enthalpy difference LMED method [32] is used. This method is adequately used in the present case, where the dehumidifier is considered as a shell and tube heat exchanger with a single pass. The applied balance across the condenser is shown below.

$$m_{cw}c_{cw}(T_{cw2} - T_{cw1}) = UA_{DH}\Delta T_{lm} \tag{30}$$

where ΔT_{lm} is calculated as:

$$\Delta T_{lm} = \frac{(T_{a2} - T_{cw2}) - (T_{a1} - T_{cw1})}{ln\left(\frac{T_{a2} - T_{cw2}}{T_{a1} - T_{cw1}}\right)} \tag{31}$$

3.4. System Key Performance Parameters

3.4.1. Humidifier Efficiency

This factor shows the capability of the humidifier to transfer the amount of water vapor, compared to that in the full saturation condition. It indicates the performance of the design, along with the packing, and can be calculated as follows:

$$\eta_H = 100\left(\frac{\omega_{a2} - \omega_{a1}}{\omega_s - \omega_{a1}}\right) \tag{32}$$

The energy-based effectiveness of the humidifier is a non-dimensional value, which can evaluate the humidifier performance based on the maximum possible change in the total enthalpy rate. The energy effectiveness is calculated based on the following [36]:

$$\varepsilon_{HD} = \frac{m_a c_a (T_{a2} - T_{a1})}{C_{min}(T_{a1} - T_{w1})} \tag{33}$$

3.4.2. System Gain Output Ratio (GOR)

The solar energy is used in this system as the heating source. The yield from the desalination is the amount of distillate produced; hence, the yield over the input energy to the system represents the gain output ratio of the system:

$$GOR = \frac{m_d h_{fg}}{Q_{in}} \tag{34}$$

3.4.3. Humidifier Thermal Efficiency

In order to measure the energy conversion in the humidifier, the input energy to the system is related to the output from the humidifier. It indicates how much thermal energy is lost in the humidifier and not being used for the purpose of humidification:

$$\eta_{T_{HD}} = 1 - \frac{Q_{out_{HD}}}{Q_{in}} \tag{35}$$

$$Q_{out_{HD}} = m_a c_a (T_{a2} - T_{a1}) + m_a (\omega_{a2} - \omega_{a1}) c_w T_d \tag{36}$$

3.4.4. Convective Heat and Mass Transfer Coefficients

The ratio of the convective heat transfer coefficient to the convective mass transfer coefficient represents the amount of heat per unit volume required to raise the temperature by one degree. This ratio is affected by the type of process components, insulation and air/water stream flow variations. The ratio is calculated from the Chilton–Colburn analogy [26]:

$$\frac{h_H}{h_M} = \rho_a c_a \left(\frac{Sc}{Pr}\right)^{\frac{2}{3}} \tag{37}$$

where

$$Sc = \frac{\mu_a}{\rho_a D_{water/air}} \tag{38}$$

The diffusivity of water in the air is calculated by the following relation [37] in the temperature range of 273 $K < T < 373$ K:

$$D_{water/air} = 1.97 \times 10^{-5} \left(\frac{T_{a_{avg}}}{256}\right) \tag{39}$$

3.5. Thermodynamic Relations

The properties of the fluids are calculated using the thermodynamic relations. The following relation calculates the absolute humidity [38]:

$$\omega = 0.62 \frac{P_v}{P_T - P_v} \tag{40}$$

The partial pressure P_v of water vapor is calculated from Antoine equation [39]:

$$ln\ P_v = 18.3036 - \frac{3816.44}{227.02 + T(^oC)} \tag{41}$$

The humid air enthalpy is calculated by [38]:

$$H_a = [c_a T_a + 597.2\omega] \times 4186.8 \quad (42)$$

The specific heat of humid air c_a [39] is obtained from the following relation:

$$c_a = [0.24 + 0.46\omega] \quad (43)$$

3.6. Process Economics

The preliminary economic analysis is based on the experiment cost information obtained during the construction process. The capital investment data, including the installation, are collected and shown in Table 3, which can be used for the production cost analysis.

Table 3. Capital cost of the HDH unit.

Description	Cost	
HDH desalination system	2600	US$
Oil tank and circulation system	350	US$
Control unit and sensors	750	US$
Solar concentrator system	5000	US$
HDH Capital cost (P)	8700	US$

The summation of fixed and variable operation costs gives the cost of the production, where the total operation cost will include the operation, maintenance, and the annual capital cost for the process, which can be obtained by the following relation [40]:

$$C_{TOP} = C_A + C_{OP} + C_M \quad (43)$$

The maintenance cost is taken as 3% [41,42] of the annual capital charges, which can be less than 2%, as estimated by El-Dessouky et al. [43]. The uniform series of payment method is used to calculate the annual capital cost (C_A). The capital recovery of the project, invested at a 5% interest rate for 20 years, is obtained from the following relation, as an annualized form [44]:

$$Anual\ capital\ cost\ (C_A) = P\frac{[i(1+i)^n]}{[(1+i)^n - 1]} \quad (44)$$

The calculations accounted for the variable operating cost, which is influenced by the price of the energy consumed by the process in the drives and control system. The local energy price is 0.048 US$/kWh [45], as the standard price for the industrial sector in Saudi Arabia. The unit is assumed to operate 10 h per day, with the availability of 90% of the year. The following relation is used to calculate the production cost:

$$Production\ cost = \frac{Total\ production\ cost\ (C_{TOP})}{Annaul\ production}\frac{US\$}{m^3} \quad (45)$$

4. Results and Discussion

The system was operated and tested to evaluate the key performance factors and the productivity at different operating conditions.

4.1. System Productivity

The HDH unit productivity is affected by the circulating air to water ratio as well as by the circulating oil flow rate for the designed solar-driven process. The process has been tested at different

air flow rates with a constant oil flow over a certain time period; then, the oil flow rate is changed, and the air flow is set to the next desired testing flow rates. System productivity, at different air and oil flow rates, is illustrated in Figure 10. The objective of increasing the air flow rate is to obtain the highest entrained water in the air at the maximum efficiency of the humidifier in order to separate them by condensation in the dehumidifier section. The maximum obtained system productivity is 24.31 kg/day at the air flow of 0.0631 kg/s. This productivity is enhanced by the oil flow of 0.0983 kg/s, which delivered the thermal energy to the humidifier at the maximum balance between the incoming solar irradiance and the air cooling effect in the humidifier. Moreover, the effect of increasing air flow rate on the productivity, which shows a reduction in the process yield when the air flow rate is increased, is presented in Figure 10.

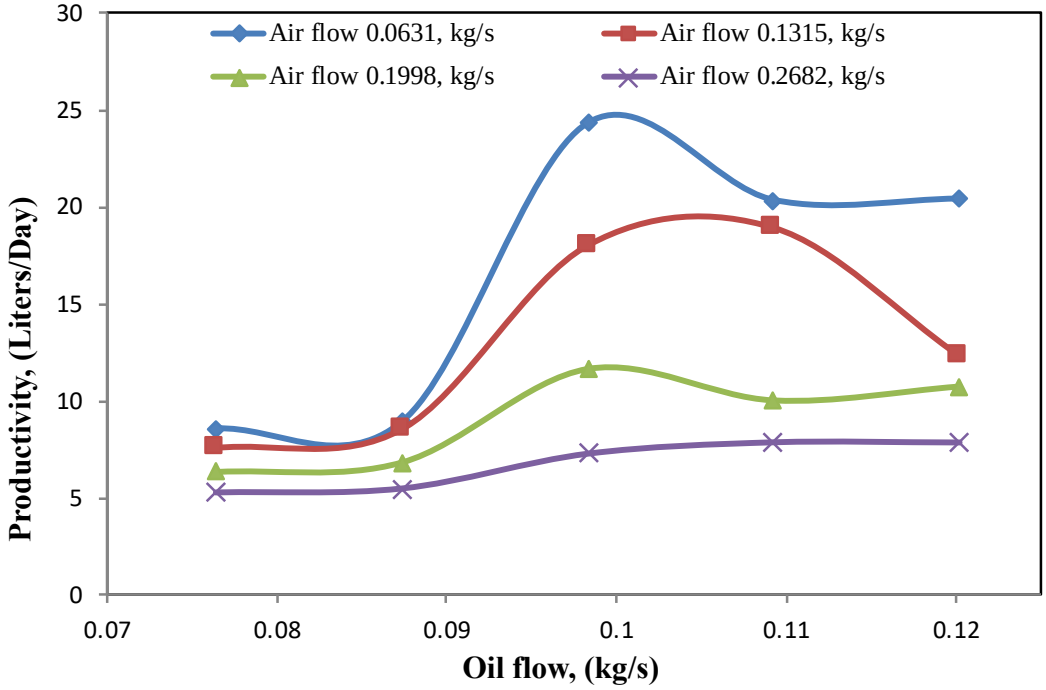

Figure 10. The productivity of the system at different air and oil flow rates.

At a circulating oil flow rate of 0.0983 kg/s, the highest yield is obtained. The productivity of the system is reduced by 26% when the air flow increased to 0.1315 kg/s and further decreased by 52.2% and 70.1% at air flow rates of 0.1998 kg/s and 0.2682 kg/s, respectively. The circulating water temperature has a significant role in the humidifier performance, where the system's highest productivity is obtained at a circulating water temperature of 49.23 °C. The circulating water temperature is decreased when the circulating air flow rate increases, and the maximum reduction was 21.7% at the highest air flow rate. The experimental output is shown to have some fluctuations due to many factors that interfere with the process stability, such as the climate conditions and characteristics of the independent components. In general, each tested condition shows a trend in the process behavior despite the fluctuation rate, which indicates the system outcome. The heat input on the bottom heater of the humidifier provokes the productivity of the system by increasing the humidifier circulating water temperature, which is shown in Figure 11. In the humidifier unit, the highest oil temperature is achieved when the unit performance is combined with the oil flow rate, achieving the required energy input for the maximum circulating water temperature. Increasing the oil flow positively affects the process productivity until the point of the tradeoff between either the installation of an enormous humidifier heat exchanger or a larger solar concentrator aperture area. The reduction of heating at higher oil flow rates is attributed to many factors, such as the absorber heat removal coefficient and less resident time of the oil flows inside the absorber tube and humidifier heat exchanger.

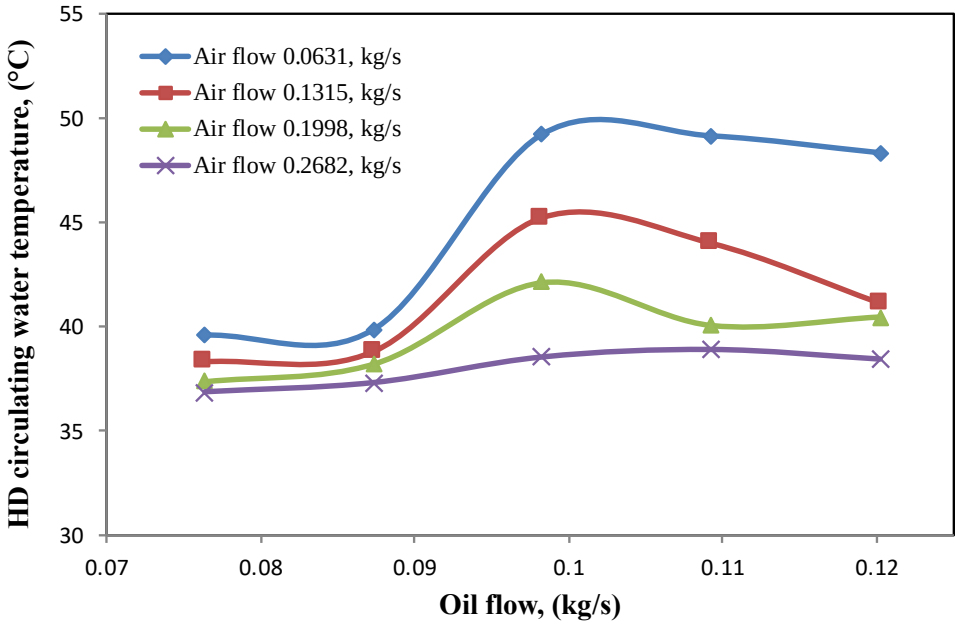

Figure 11. Average HD water temperature at different air and oil flow rates.

4.2. Energy of the System

Based on the oil circulation flow rate, the solar energy gain varies; hence, the input energy to the heat exchanger on the bottom of the humidifier is affected by this variation. The circulating air entering the humidifier has the effect of cooling the system, which has lost the sensible heat in the dehumidifier. The energy input to the heat exchanger on the bottom of the humidifier is illustrated in Figure 12. In the present system, the energy input increased, in most cases, as the oil circulation rate increased up to the desired heating condition, which ranges from 2.39 to 3.07 kWh at an oil flow of 0.0983 kg/s. At a higher humidifier air flow rate, the bottom heat exchanger did not yield the required input energy, and the energy supplied was reduced by 39.3% at the maximum oil flow rate compared to the highest obtained air flow rate of 0.0631 kg/s.

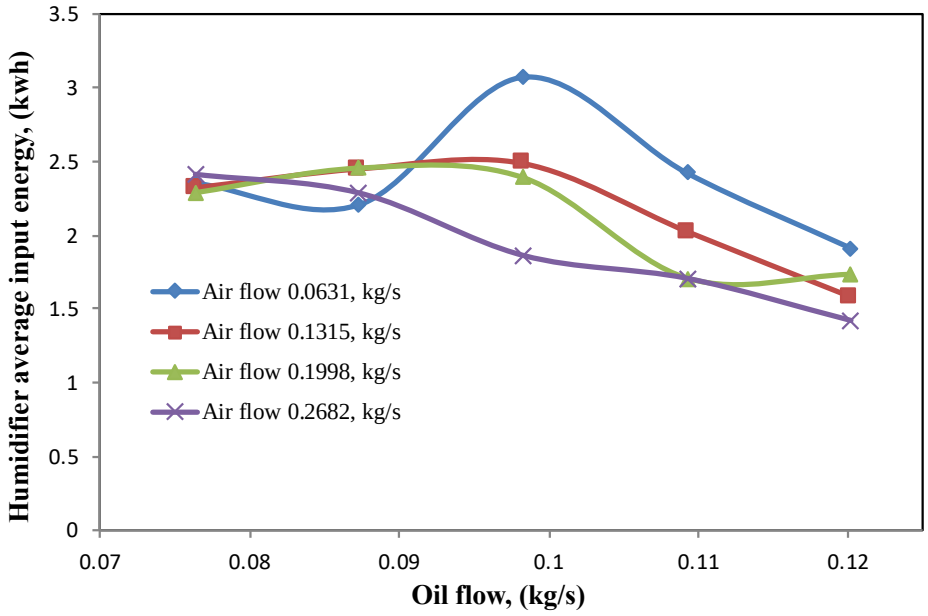

Figure 12. HD average input energy at different air and oil flow rates.

4.3. The GOR

At the low oil flow rate, the process revealed no significance in the unit productivity compared to the high oil flow rates. The variation of the averaged GOR versus oil flow rate of the desalination unit, under the tested conditions, is illustrated in Figure 13. The GOR was increasing at a higher oil flow rate due to the increase in the supply of the thermal energy from the solar concentrator. Additionally, the GOR decreases at a higher circulating air flow rate due to the enhanced cooling effect on the process. Moreover, at oil circulations of 0.984 kg/s and lower, the unit GOR and productivity was significantly reduced, and the process output was adversely affected.

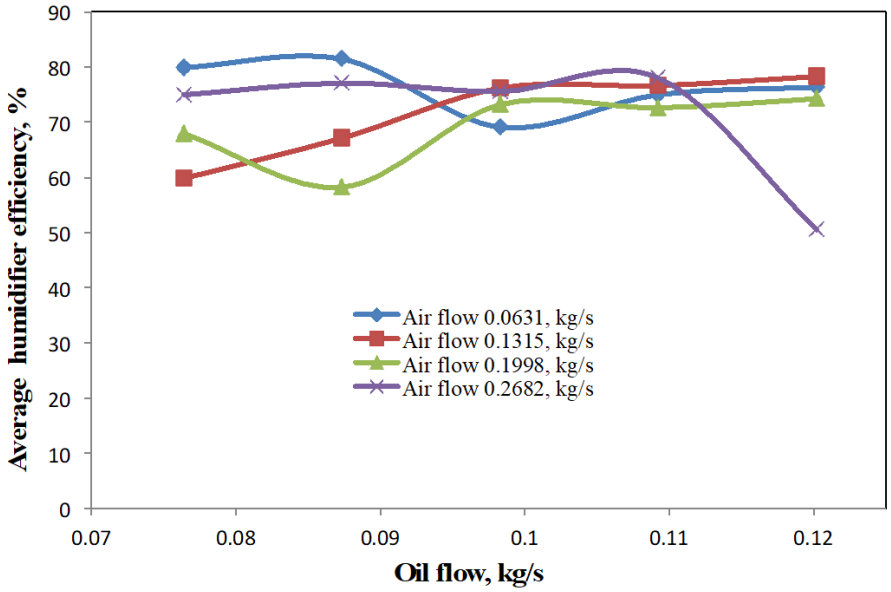

Figure 13. HD average input energy at different air and oil flow rates.

The circulation rates of the oil and air are shown to have higher GORs at an oil flow rate of 0.1202 kg/s, and the process GOR is higher at the lowest circulating air flow rate of 0.0631 kg/s compared with other tested conditions.

4.4. Humidifier Efficiency and Thermal Efficiency

The humidifier efficiency is linked to the design, packing type and air-to-water ratio. All these parameters are reflected on the mass transfer coefficient and therefore shown in the performance efficiency of the humidifier. The variation of the humidifier efficiency at different air to water flow ratios and different heat input conditions, represented by oil flow rates, are shown in Figure 14. The amount of vapor transferred is above 60%, compared to the ideal saturated condition, in order to humidify the air. The thermal efficiency of the humidifier, where the performance appears to be lower when the oil flow rate increases to 0.0983 kg/s and above, is shown in Figure 15. The humidifier has the efficiency of 78% and above to deliver the energy from the heat input to the coldest part, which is the humid air in this condition.

The humidifier average energy-based effectiveness for all cases is shown in Figure 16. At higher circulating air flow rates, the energy-based effectiveness is shown to be decreased. Air flow rate has an influence on the cooling of the system and reduces the actual heat transfer rate. Therefore, a further energy supply is required. For all cases, increasing the oil flow rate has an insignificance effect of energy-based effectiveness reduction compared to the increase to the circulating air flow rate. At the highest test air flow of 0.2682 kg/s, the average energy-based effectiveness is shown to be from 0.4 to 0.476.

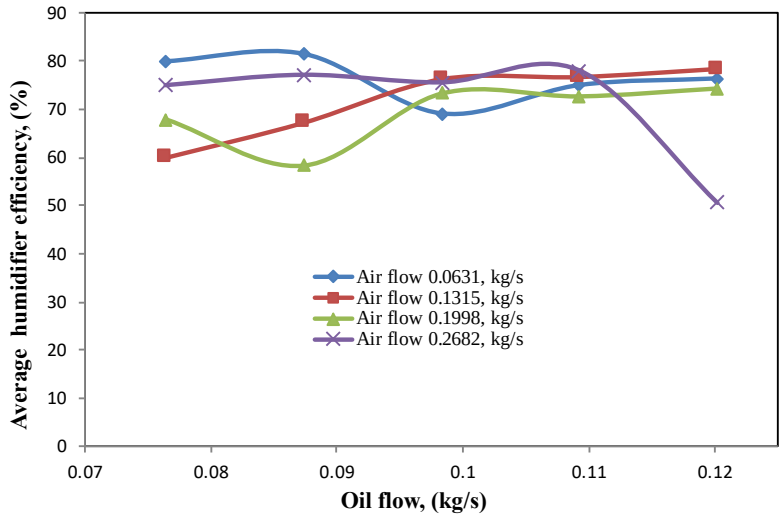

Figure 14. Average humidifier efficiency at different air and oil flow rates.

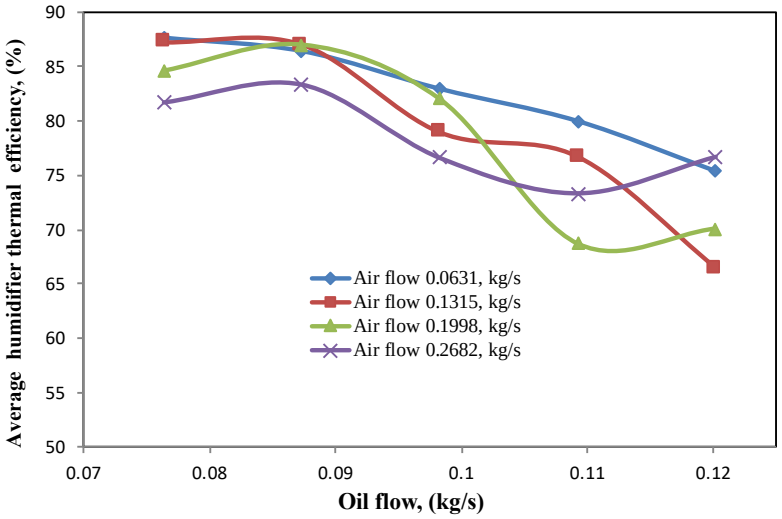

Figure 15. Average humidifier thermal efficiency at different air and oil flow rates.

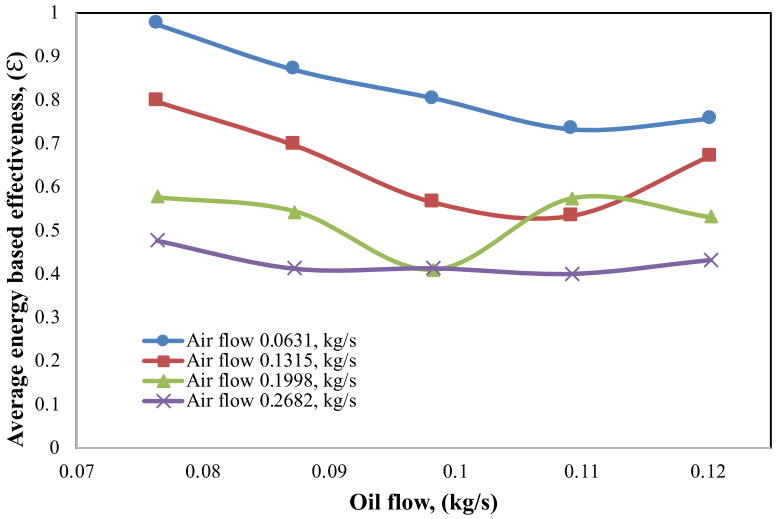

Figure 16. Average energy-based effectiveness ε at different air and oil flow rates.

4.5. Enthalpy Difference

The enthalpy of the humidifier outlet is the combination of the enthalpy of the dry air and the enthalpy of the entrapped water vapor within the stream. The outlet enthalpy is measured relative to the inlet air enthalpy in the humidifier. The calculated enthalpies are related to the specific and latent heats at the operating temperature and the amount of vapor in the streams, which have been computed by Equation (42). The enthalpy difference of the humidifier, at different operating air flow rates and different circulating oil flow rates, is illustrated in Figure 17.

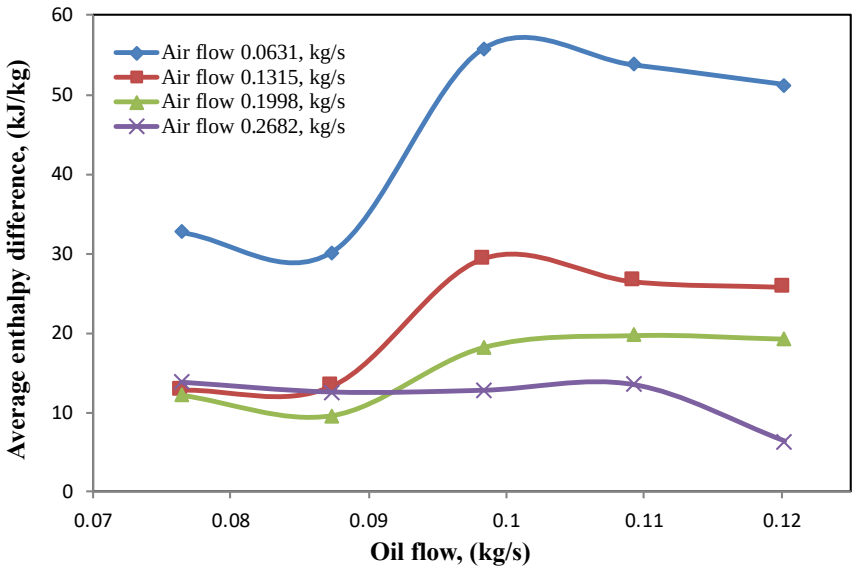

Figure 17. Average enthalpy difference at different air and oil flow rates.

At lower air flow rates, the enthalpy difference of the system is shown to be greater, and the oil circulation rate of 0.0983 kg/s is shown to increase the enthalpy difference for most of the air streams.

4.6. Humidifier Mass Transfer Coefficient

The average mass transfer coefficient of the experiment is plotted against the oil flow rate and is shown in Figure 18. The effect of both heating and air/water circulation on the coefficient is shown in this figure. The air–water flow rate significantly affects the value of the mass transfer coefficient during all experimental runs. Increasing the air flow rate reveals an increase of the mass transfer coefficient up to the air flow of 0.2682 kg/s, at which point the coefficient declined due to concentration and heat potential complications. The process is known to have a mass transfer due to the concentration difference on the airside of the interface and latent heat potentials. The mass transfer coefficient is calculated from Equation (26), in which the process driving force is expressed in terms of the enthalpy difference, where the enthalpy is a thermodynamic property calculated using Equation (42). Hence, the driving force is the function of both temperature and humidity. The variation of the circulating oil flow changes the heating input to the humidifier, which is reflected in the mass transfer behavior. The air-to-water ratio affects the humidity in the system and dominantly controls the mass transfer coefficient values, where the temperature influences the system efficiency when further heat is introduced. At air flow rates of 0.0632 and 0.2682 kg/s, the system could not gain the required heating due to an insufficient air flow, low air flow rate or excessive air flow, which led to a cooling effect at higher air flow rates.

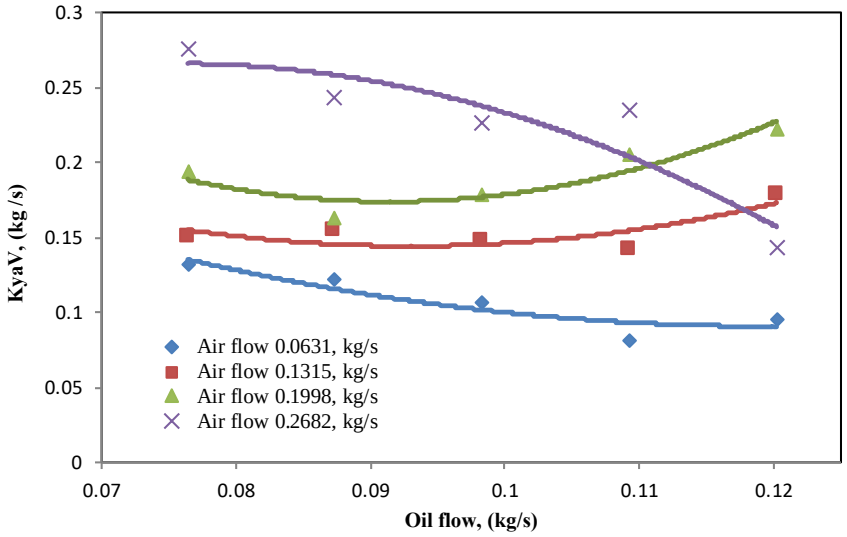

Figure 18. Average HD mass transfer coefficient at different air and oil flow rates.

4.7. Convective Mass Transfer Coefficient

The convective heat to mass transfer coefficient plot, where the coefficient increases as the air flow rate increases, is shown in Figure 19. At lower air flow rates, this ratio decreases when the oil flow rate reaches 0.0983 kg/s, at which point maximum productivity is obtained. This indicates the reduction in the thermal loss and the usefulness of the heat for enhancing the humidifier-driving force through the mass transfer controlled by the humidity difference. At a lower oil flow rate, the process either loses heat or has an insufficient heat input due to higher air flow rates. The air flow rate at 0.2682 shows a higher ratio trend, which can be further improved by using a higher-grade insulation material to enhance the process productivity at higher air flow rates and avoid heat loss. For the present system, the productivity was shown to have declined when the air increased to this limit; hence, optimization is considered a practical case, which could be implemented in order to obtain a tradeoff between the cost, productivity, and size for a good performance. The best unit performance was obtained at the lowest tested air flow and the point at which the oil flow reached 0.0983 kg/s, where the lower loss was obtained per unit volume.

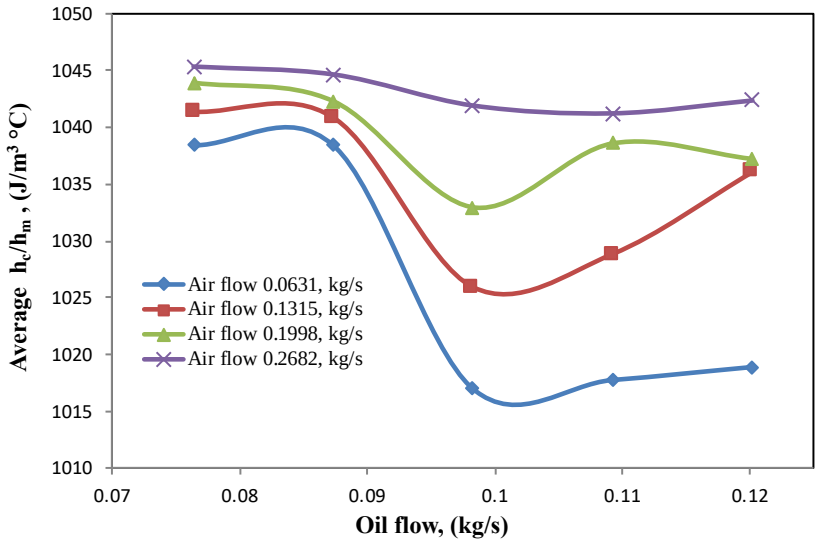

Figure 19. Average HD convective heat and mass transfer coefficient ratio at different air and oil flow rates.

4.8. Optimum Condition

The results of the experiment are analyzed in terms of productivity, production cost and GOR in order to find the best operating conditions that meet the process economics with a high yield. The behavior of the process at different circulating oil and air flow rates, obtaining a tradeoff between the maximum productivity, production cost, and the GOR, is illustrated in Figure 20. Under all operating conditions, the process reveals a high productivity and GOR, with the lowest operating cost, at a circulating oil flow of 0.0983 kg/s. The maximum productivity obtained is 24.31 kg/day at a circulating air flow rate of 0.0631 kg/s, and the GOR is found to be 0.51. This condition has the minimum operating cost, where the production cost attained is 12.54 US$/m^3, which is 0.0125 US$/liter. Since the process used solar energy for heating, the heating energy cost would not affect the unit production cost, although the capital investment would. The process economics can be improved by the reduction of the system capital investment, such as automation and controls, since the system works at low pressures and temperatures, or by increasing the productivity by enhancing the power utilization using an auxiliary heating system operated by solar photovoltaic (PV) panels. The general output of the process reduces as the circulating air flow rate increases. At the highest air flow rate, the economics of the process is found to be discouraging, with a production cost of 38.92 US$/m^3 under the optimal circulating oil condition. Similarly, the GOR of the process has a tendency toward further reduction when the circulating air flow rate is increased. There is also uncertainty in the operating variables due to the variation during different seasons throughout the year, which could affect the overall system results, but the process is expected to behave in a manner similar to the results obtained. The more expensive design may allow for a higher circulating oil temperature of the parabolic concentrator, which requires a larger heat exchanger surface area or humidifier air and water contact area; hence, the benefits could require a higher system capital cost. The maximum output of the experiment, compared with the previous work in the field of solar desalination using the HDH method, is presented in Table 4. Despite the design and capacities of the processes in other research work, the process design in the present study has economic improvements, which enhance the commercialization potential of the process, as demonstrated in Table 4.

Table 4. Comparison between the current result and previous work.

Reference	Description	Productivity, L/day	Cost, US$
Sharshir et al. [46]	Hybrid solar HDH and solar stills with evacuated solar water heater.	66.3	0.034
Zhani et al. [47]	Flat plate air solar collector and flat-plate water solar collectors with HDH unit.	20	0.093
Hamed et al. [23]	Evacuated tube water solar collector with HDH unit.	22	0.0578
Deniz et al. [48]	Solar air heater and solar water heater with HDH unit.	10.87	0.0981
Zubair et al. [49]	Solar evacuated tubes with HDH unit.	46.59	0.036
Behnam et al. [50]	Solar desalination system equipped with an air bubble column humidifier, evacuated tube collectors and thermosyphon heat pipes.	6.275	0.028
Current work	Solar PTC with HDH unit.	24.31	0.0125

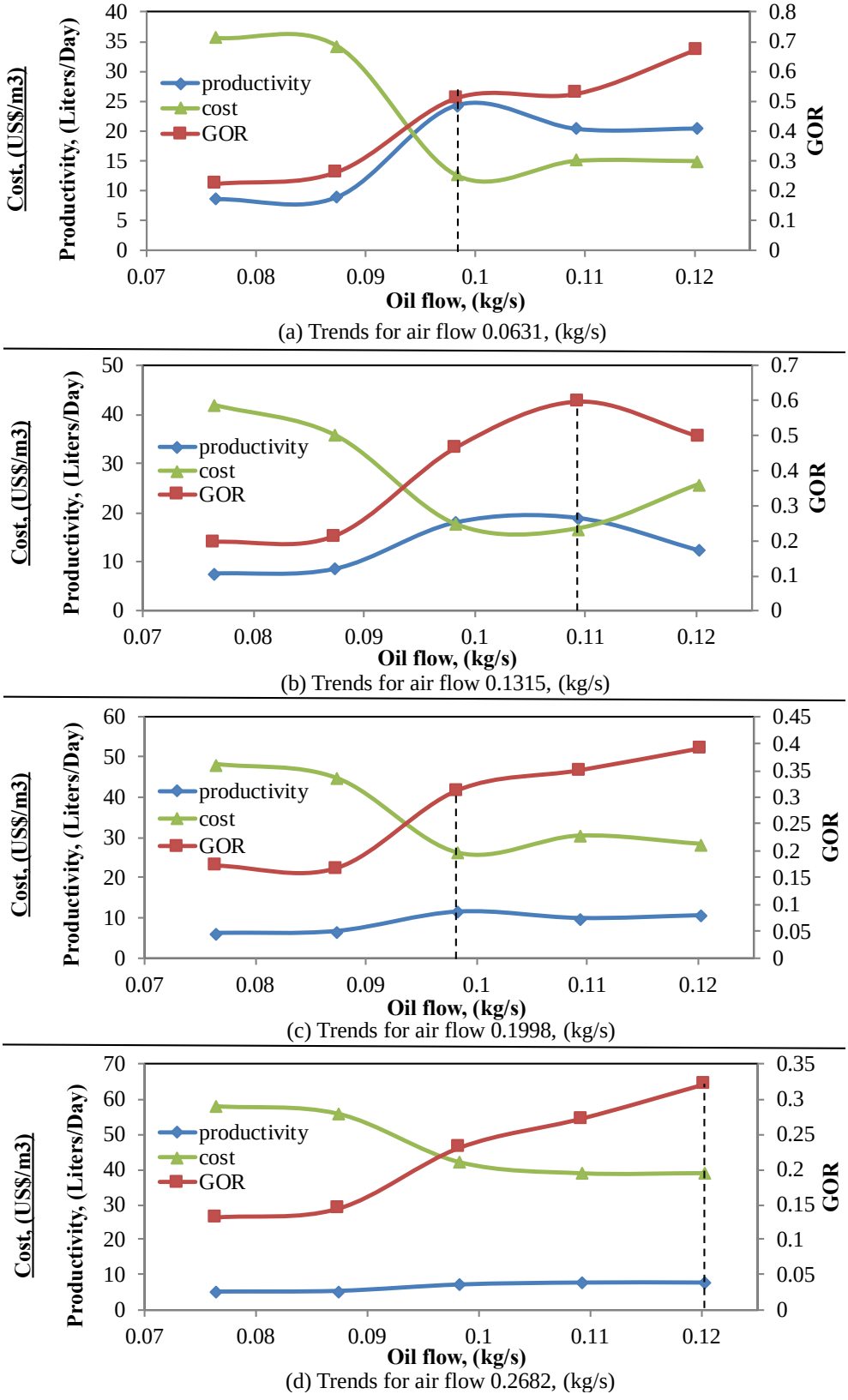

Figure 20. System optimization at different air and oil flow rates.

4.9. Collector Efficiency

The behavior of the averaged efficiency of the PTC under the operating conditions is illustrated in Figure 21. A decrease of the instantaneous efficiency of the PTC, following the increase of the circulating oil flow rate, is shown in this figure. The low efficiencies at high circulating oil flow rates, attributed to the shorter residence time of oil in the absorber tubes, reduce the heat gain of the PTC. The circulating water temperature lines of the humidifier, shown in Figure 19, illustrate the condition of the humidification process within the operating oil flow, where the lower oil flow revealed a lower productivity and high PTC efficiency. Moreover, the temperatures of the circulating water in the humidifier were found to be higher at the oil flow rate of 0.0983 kg/s than with other settings, which shows the optimum oil flow rate for the heat exchange in the humidifier. The average PTC efficiency at the lowest oil flow rate is 27.8% and is reduced by 49.5% at the maximum flow rate.

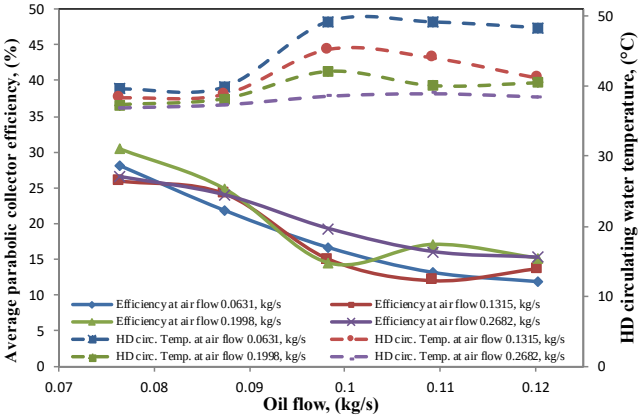

Figure 21. Average collector efficiency at different air and oil flow rates.

In the designed system, the ratio of the heat gained to the amount of beam radiation concentrated in the absorber tube is revealed to be higher, especially from the middle to the end of the solar day due to closed system circulation. Moreover, for all of the cases in which the incidence angle increased throughout the day, the losses due to the end effect decreased; hence, the PTC efficiency increased. When the beam radiation reduced at the end of the day, the system still can deliver the energy to the humidifier at a higher rate due to the stored heat in the oil expansion tank and the circulating air and water of the humidifier. The behavior of the circulating oil inlet and outlet temperatures in the parabolic concentrators is shown in Figure 22. Generally, at higher oil flow rates, the system heat storage capabilities increased due to multiple circulation procedures. This positively affects the value of the parabolic concentrator efficiency; hence, the minimum beam radiation utilization is obtained.

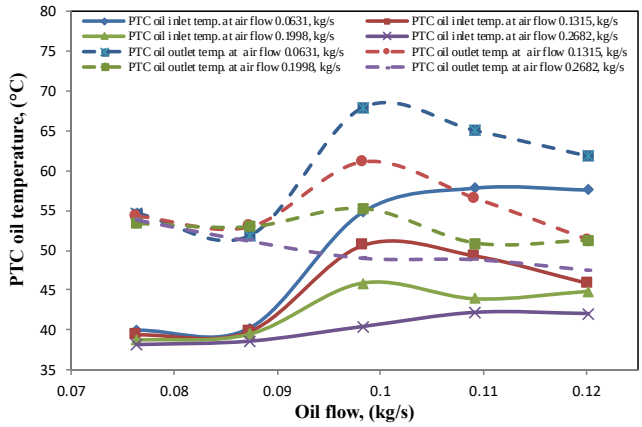

Figure 22. Average PTC oil temperature at different air and oil flow rates.

The heat removal factor F_R is known to be the measure of the thermal resistance by the absorbed radiation in the circulating oil [27]. The heat removal factor changes at different oil and air flow rates, as shown in Figure 23. At very high oil flow rates, it possible that the oil outlet temperature becomes closer to that of the inlet; therefore, the factor is reduced. From the figure, at the highest oil flow rate of 0.12 kg/s, the oil temperature difference decreases and reduces the heat removal factor. In all the tested cases, the oil flow rate of 0.0983 kg/s was shown to have high system productivity and maintained oil temperature difference, and the higher air flow rates revealed higher values of the heat removal factor.

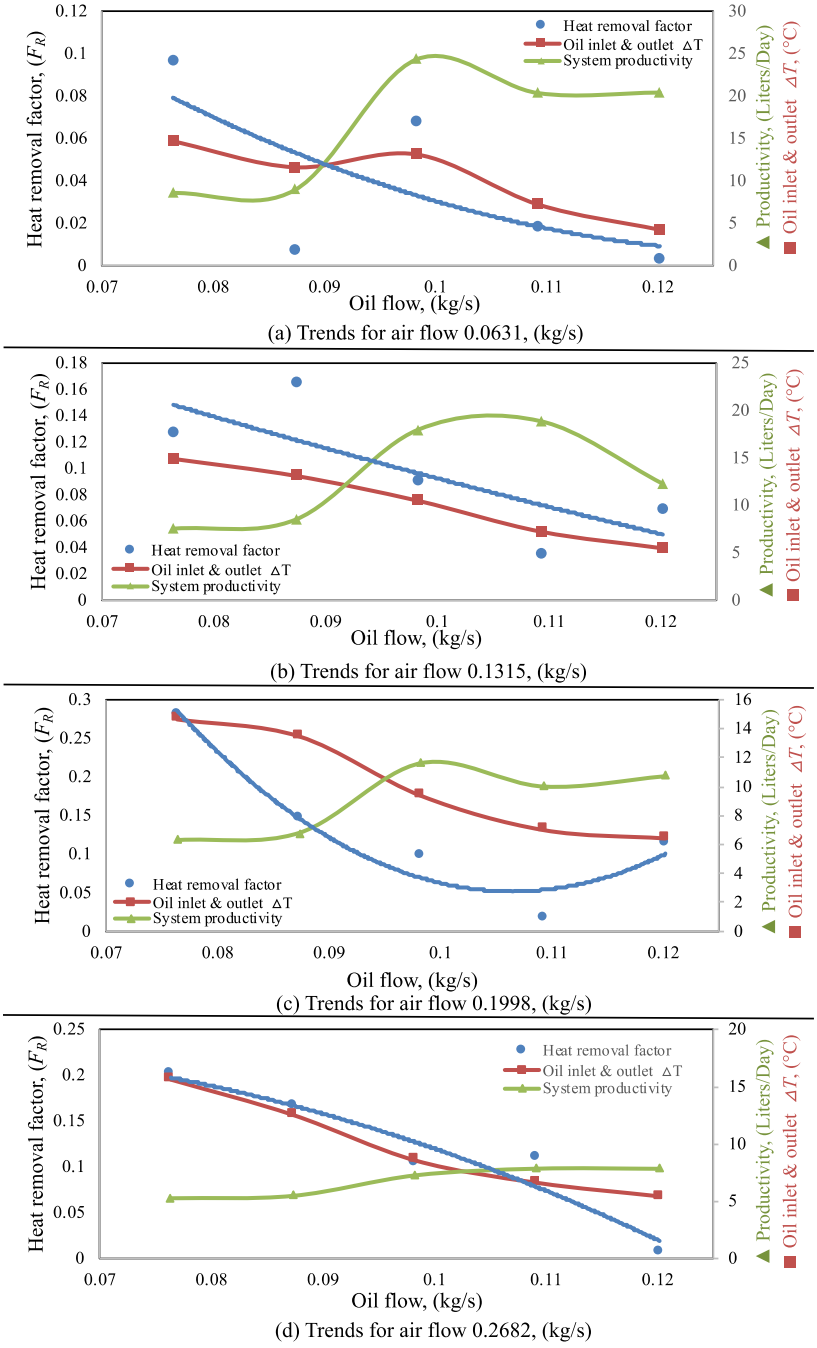

Figure 23. Heat removal factor F_R of the PTCs with the change of system productivity and oil ΔT at different air and oil flow rates.

4.10. Absorber Tube Overall Heat Transfer Coefficient

The overall heat transfer coefficient, including the absorber tube wall, calculated using the heat removal factor, the heat removal coefficient and the convective heat transfer coefficient inside the absorber tube, is obtained from the recorded experimental data. The behavior of the overall heat transfer coefficient, at different circulating oil flow rates and humidifier air flow rates, is illustrated in Figure 24. The circulating oil inside the tube is found to be laminar in all the tested flows, and the corresponding Nusselt number was 4.364. The overall heat transfer coefficient depends on the conduction through the tube wall, the convection inside the tube and the heat removal loss coefficient, and the ambient conditions, such as the wind speed and temperature, influence its value. The convection coefficient for the laminar flow has less significance for the value of the overall heat transfer coefficient, and the wall conduction coefficient does not have an impact on changing the overall heat transfer coefficient. Therefore, the calculated heat removal coefficient profoundly influences the process affected by the ambient conditions. Increasing the circulating oil flow rate will increase the tendency toward a higher heat loss; hence, the overall heat transfer coefficient will increase. At a lower air flow rate, such as 0.0631 kg/s, the absorber tube will gain more heat at a lower oil residence time inside the absorber tube; hence, the system will have a tendency to increase the heat removal coefficient. The heat removal value could be decreased using a glass vacuum tube instead of a PTC glass cover.

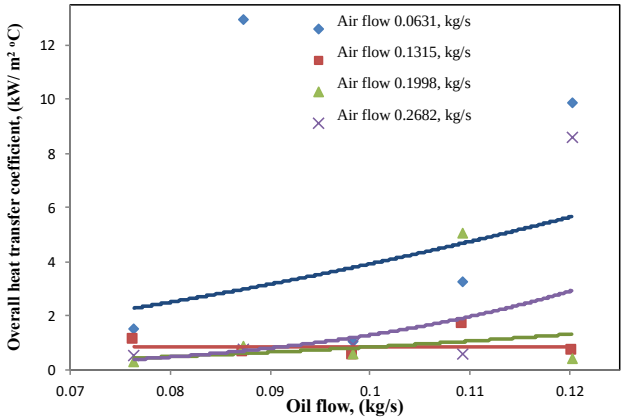

Figure 24. Average absorber tube overall heat transfer coefficient.

5. Conclusions and Recommendations

5.1. Conclusions

This work has integrated modeling, techno-economic analysis, design, and experimental work for the assessment and optimization of a solar-driven humidification and dehumidification desalination unit for arid areas. The system is characterized by high efficiency, relatively simple operation and low maintenance. The GOR of the process, considering the primary purpose of the system construction, would have less priority compared to the other studied factors. Solar energy, concentrated by a PTC system, and an associated HDH desalination unit have been studied in order to evaluate the system productivity, efficiency, and economic feasibility. The design, construction, and testing have been implemented, and the following results have been obtained for a case study in Saudi Arabia:

- The HDH system productivity is significantly influenced by the circulating air-to-water flow ratio, and the highest system productivity obtained is 24.31 kg/day. The best productivity curve for all the tested air flow rates is obtained at a 0.0983 kg/s circulating oil flow rate. The system showed a drastic reduction in productivity of 70.1% when the air flow rate increased to 0.2683 kg/s.
- Increasing the humidifier circulating water temperature positively affects the humidifier productivity. This has been achieved by modulating the heat input to the humidifier by altering

the oil circulation through the PTCs. The maximum humidifier circulating water temperature with the highest productivity is 49.23 °C. The circulating water temperature is reduced by 21.7% when the highest circulating air flow rate of 0.2683 kg/s is achieved.

- Increasing the circulating oil flow rate positively influences the system's productivity until the point when this starts to decline; hence, a tradeoff between either a larger size humidifier heat exchanger or larger PTC surface area is required to enhance productivity.
- The energy consumption of the process under the best conditions varies between 2.39 and 3.07 kWh, and the energy delivered to the humidifier is decreased, when further circulating oil flow is increased, and reached a 39.3% reduction at the highest oil flow rate.
- The humidifier efficiency ranges between 69.1% and 75.6%, and the thermal efficiencies are in the range of 76.6% and 82.94% at a circulating oil flow rate of 0.0983 kg/s.
- The cost analysis of the system indicates a reduction of the production cost under the highest productivity condition. A tradeoff between the cost, productivity, and GOR is necessary. The production cost is 12.54 US$/m^3 under a condition where the highest GOR of 0.51 is obtained, and the maximum productivity is achieved.
- The efficiency of the PTCs is calculated, and the results showed a significant increase in the performance at a low circulating oil flow rate. The oil circulation procedure in a closed loop enhances the system efficiency by reducing the losses and enhancing the energy storage in the oil expansion tank.

Finally, the PTC coupled with the HDH desalination system reveals a promising desalination technique in arid areas, where no commercial desalination plants are available for a small population. The system outcome can be improved by the further development of a hybrid system of PV, PTC, and auxiliary heaters in combination with an HDH desalination unit.

5.2. Recommendations for Future Work

The solar-driven HDH desalination process would be more effective, with a higher performance, cost-efficient and positive environmental impact in the desalination technology, if the following recommendations were implemented.

- The solar-driven HDH system can be coupled with other thermal desalination technologies to increase the desalination process yield. The dual-purpose plants for power and desalination can be significantly improved. The optimization of the dual-purpose system can benefit from and be enhanced using a shortcut method to address the need for conceptual design studies [51]. Moreover, decoupling the mass balances and the heat balances and heat-transfer sizing equations using the linear programming (LP) optimization formulation simplifies the computations and significantly reduces the model size and complexity [52]. A hybrid design can include both thermal and reverse osmosis plants [53]; therefore, economic optimization can be carried out in the overall system to identify the process configuration tradeoffs in various scenarios. Mixed-integer nonlinear programming (MINLP) is used for 20 RO membrane modules, and 58% of savings in freshwater use is achieved as compared to the existing base case operations [54]. The solution to this program provides the optimal arrangement, types, and sizes of the reverse-osmosis units and the booster pumps [55]. Such an application showed an improvement in the optimization, determining the optimal mix of solar energy, thermal storage, and fossil fuel to attain the maximum annual profit of the shale gas production system studied [56], which can be applied to the solar-driven HDH system studied.
- Heat integration can be performed to reduce the operating cost by coupling the HDH desalination system to industrial facilities. This approach has been implemented along with the optimization of multi-effect distillation (MED) and membrane distillation (MD) and revealed a successful cost reduction in different scenarios [57]. Moreover, coupling multi-stage flash (MSF) with MED desalination processes was shown to improve the system output due to the use of the waste heat

recovery [58]. Therefore, the HDH desalination can be integrated with solar collectors, absorption refrigeration cycles, and organic Rankine cycles.

- The existing desalination systems can consider the HDH as a modular desalination technology in the retrofitting option, which increases the capacity of the output [59].
- The economic factors are the most important factors relating to project improvement; hence, the low cost-integrated solar HDH desalination system is an option that incorporates sustainability in the design and selection of projects. The metric approach can provide an evaluation of project profitability and promote sustainability related to the capital cost [60].

Author Contributions: Conceptualization, F.A. and M.A.; Methodology, F.A.; Software, F.A.; Validation, F.A., A.M. and M.A.; Formal Analysis, M.A.; Investigation, M.A.; Resources, F.A.; Data Curation, M.A.; Writing-Original Draft Preparation, M.A.; Writing-Review & Editing, A.M.; Visualization, F.A.; Supervision, F.A.; Project Administration, A.A.; Funding Acquisition, F.A.

Funding: This project was funded by the National Plan for Science, Technology and Innovation (MAARIFAH)—King Abdulaziz City for Science and Technology—the Kingdom of Saudi Arabia—award number (11-ENE2004-03).

Acknowledgments: The authors also acknowledge, with thanks, the Science and Technology Unit, King Abdulaziz University for their technical support. The authors acknowledge the great support of Abdulsalam Alghamdy, head of the King Salman Energy chair, in accommodating the project installation in their premises.

Conflicts of Interest: The authors declare no conflict of interest.

Nomenclature

A	Surface area, m^2
A_a	Total aperture area, m^2
A_e	Lost area due to end effect, m^2
A_f	Geometric ratio, m^2
A_l	Lost area, m^2
C	Collector concentration ratio
C_A	Annual capital cost, US$
C_M	Maintenance cost, US$
C_{OP}	Operating cost, US$
C_r	Heat capacity ratio
C_{TOP}	Total operating cost, US$
D_{AB}	Mass diffusion coefficient of air in water, m^2/s
D_i	Inside diameter, m
D_o	Outer diameter, m
F_R	PTC heat removal factor
G_{bn}	Normal beam radiation, W/m^2
H	Enthalpy, kJ/kg
I	Solar irradiance, W/m^2
K_y	Gas phase mass transfer coefficient of humidifier, Kg/m^2 s
L	Latitude angel, degrees
N	Number of the day in the Gregorian year
Nu	Nusselt number
P	Capital cost, US$
Pr	Prandtl number
P_T	Total pressure, mmHg
P_v	Vapor pressures, mmHg
Q_{in}	Heat transfer rate, W
Re	Reynolds number
Sc	Schmidt number
T_a	Air temperature, °C
T_{cw}	Cooling water temperature, °C
T_{MU}	Make water temperature, °C

T_{oil}	Oil temperature, °C
T_w	Water temperature, °C
U	Overall heat transfer coefficient, W/m^2 °C
U_c	Overall heat transfer coefficient of the absorber tube, W/m^2 °C
U_L	Heat removal coefficient of the absorber tube, W/m^2 °C
V	Volume of the humidifier, m^3
W	Aperture width, m
a	Interface area, m^{-1}
c_a	Specific heat of humid air, kJ/kg °C
c_w	Specific heat of water, kJ/kg °C
f_c	Enthalpy correction factor, kJ/kg
h	Hour angle, degrees
h_{ab}	Oil convective heat transfer coefficient, kJ/s m^2 °C
h_c	Convective heat transfer coefficient, kJ/s m^2 °C
h_{fg}	Latent heat of evaporation of water at ambient conditions, kJ/kg
h_m	Convective mass transfer coefficient, m/s
h_p	Hight of parabola, m
i	Interest rate, %
k	Thermal conductivity, W/m °C
k_{ab}	Absorber tube thermal conductivity, kJ/s m^2 °C
l	Trough length, m
m_a	Air flow rate, Kg/s
m_{cw}	Cooling water flow rate, Kg/s
m_w	Water flow rate, Kg/s
m_d	Product water flow rate, Kg/s
m_{MU}	Make up water flow rate, Kg/s
m_{oil}	Oil flow rate, Kg/s
n	Number of years
t_s	Solar time, hour
Indices	
a	Air
amb	Ambient condition
as	Saturated air
avg	Average value
DH	Dehumidifier
HD	Humidifier
lm	Log mean
m	Mean value
oil	Oil side
s	Saturated
v	vapor
w	water
Greek	
α	Altitude angel, degrees
β	Slop of the PTC surface, degrees
γ	Intercept factor
δ	Declination angle, degrees
ε	Heat exchanger effectiveness
ξ	Reflectance of the reflector
η	PTC efficiency, %
η_H	Humidifier efficiency, %
$\eta_{T_{HD}}$	Humidifier thermal efficiency, %
η_o	Optical efficiency, %
θ	The incident angle, degrees
θ_z	Zenith angle, degrees

λ_0	Latent heat of evaporation of water at base temperature, kJ/kg
μ	Dynamic viscosity, kg/m s
ρ	Density, kg/m^3
τ	Transmittance of the glass cover
ϕ	Azimuth angle, degrees
ϕ_s	Surface azimuth angle, degrees
ψ	Absorptance of the receiver
ω	Absolute humidity, kg_{water}/kg_{air}

Appendix A

The standard uncertainties for the measured data are obtained based on the type A evaluation procedure, described in the JCGM 100:2008 [61]. The standard uncertainties, obtained from the statistical analysis of the experimental data, are shown in Figure A1. The calculation is based on the set of 14 values, measured repeatedly at noon; hence, the standard deviation has 13 degrees of freedom for each measurement. The maximum standard uncertainty for the measured data is found to be 0.94.

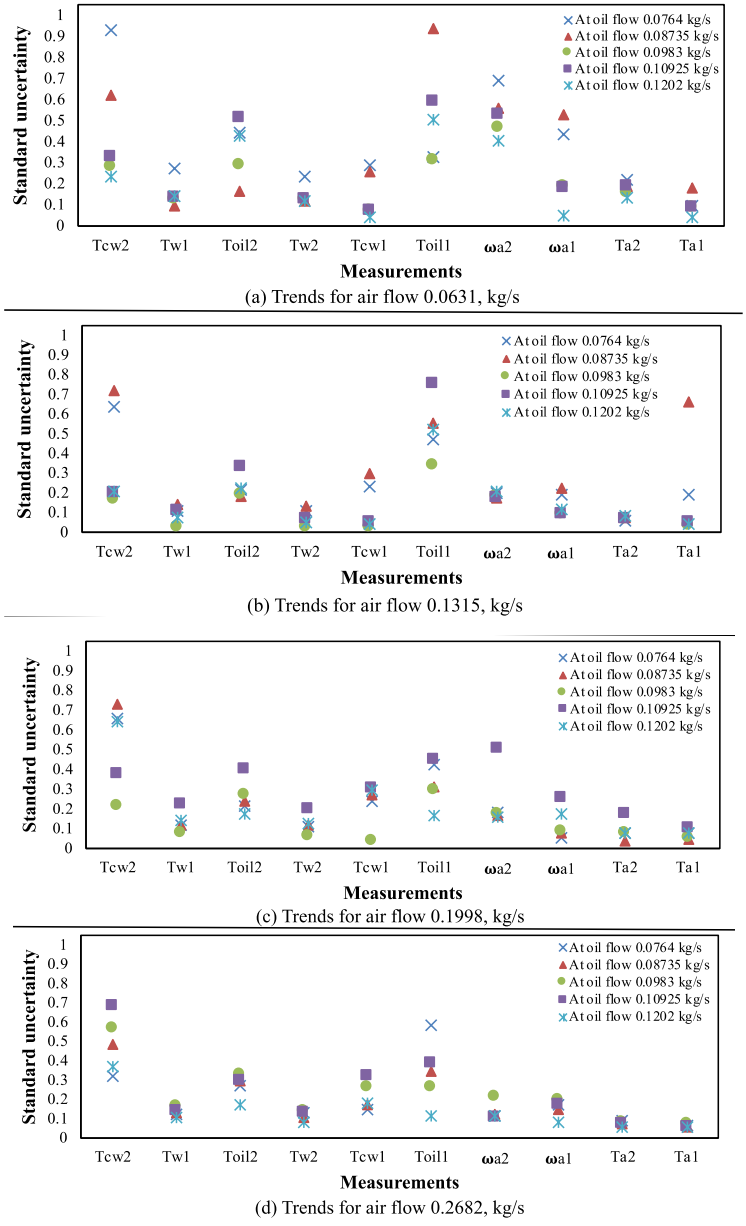

(a) Trends for air flow 0.0631, kg/s

(b) Trends for air flow 0.1315, kg/s

(c) Trends for air flow 0.1998, kg/s

(d) Trends for air flow 0.2682, kg/s

Figure A1. The standard uncertainty for the experimental measurements.

References

1. Al-Rashed, M.F.; Sherif, M.M. Water resources in the GCC countries: An overview. *Water Resour. Manag.* **2000**, *14*, 59–75. [CrossRef]
2. Almasoud, A.H.; Gandayh, H.M. Future of solar energy in Saudi Arabia. *J. King Saud Univ. Eng. Sci.* **2015**, *27*, 153–157. [CrossRef]
3. Zell, E.; Gasim, S.; Wilcox, S.; Katamoura, S.; Stoffel, S.; Shibli, H.; Engel-Cox, J.; Al Subie, M. Assessment of solar radiation resources in Saudi Arabia. *Sol. Energy* **2015**, *119*, 422–438. [CrossRef]
4. Pazheri, F.R. Solar power potential in Saudi Arabia. *Int. J. Eng. Res. Appl.* **2014**, *4*, 171–174.
5. Solar GIS, Solar Resource Maps of Saudi Arabia. Available online: https://solargis.com/maps-and-gis-data/download/saudi-arabia (accessed on 5 May 2018).
6. Tzivanidis, C.; Bellos, E.; Korres, D.; Antonopoulos, K.A.; Mitsopoulos, G. Thermal and optical efficiency investigation of a parabolic trough collector. *Case Stud. Therm. Eng.* **2015**, *6*, 226–237. [CrossRef]
7. Yassen, T.A. Experimental and theoretical study of a parabolic trough solar collector. *Anbar J. Eng. Sci.* **2012**, *5*, 109–125.
8. Murtuza, S.A.; Byregowda, H.V.; Imran, M. Experimental and simulation studies of parabolic trough collector design for obtaining solar energy. *Resour. Eff. Technol.* **2017**, *3*, 414–421. [CrossRef]
9. Jebasingh, V.K.; Joselin, G.M. A review of solar parabolic trough collector. *Renew. Sustain. Energy Rev.* **2016**, *54*, 1085–1091. [CrossRef]
10. Arun, C.A.; Sreekumar, P.C. Modeling and performance evaluation of parabolic trough solar collector desalination system. *Mater. Today Proc.* **2018**, *5*, 780–788. [CrossRef]
11. Elashmawy, M. An experimental investigation of a parabolic concentrator solar tracking system integrated with a tubular solar still. *Desalination* **2017**, *411*, 1–8. [CrossRef]
12. Zohreh, R.; Hatamipour, M.S.; Ghalavand, Y. Solar assisted modified variable pressure humidification-dehumidification desalination system. *Energy Convers. Manag.* **2018**, *162*, 321–330.
13. Mohamed, A.M.I.; El-Minshawy, N.A. Theoretical investigation of solar humidification–dehumidification desalination system using parabolic trough concentrators. *Energy Convers. Manag.* **2011**, *52.10*, 3112–3119. [CrossRef]
14. Fathy, M.; Hamdy, H.; Salem, M. Experimental study on the effect of coupling parabolic trough collector with double slope solar still on its performance. *Sol. Energy* **2018**, *163*, 54–61. [CrossRef]
15. Kabeel, A.E.; Hamed, M.H.; Omara, Z.M.; Sharshir, S.W. Water desalination using a humidification-dehumidification technique—A detailed review. *Nat. Resour.* **2013**, *4*, 286–305. [CrossRef]
16. Srithar, K.; Rajaseenivasan, T. Performance analysis on a solar bubble column humidification dehumidification desalination system. *Process Saf. Environ. Prot.* **2017**, *105*, 41–50. [CrossRef]
17. Zubair, S.M.; Antar, M.A.; Elmutasim, S.M.; Lawa, D.U. Performance evaluation of humidification-dehumidification (HDH) desalination systems with and without heat recovery options: An experimental and theoretical investigation. *Desalination* **2018**, *436*, 161–175. [CrossRef]
18. Hamed, M.H.; Kabeel, A.E.; Omara, Z.M.; Sharshir, S.W. Mathematical and experimental investigation of a solar humidification–dehumidification desalination unit. *Desalination* **2015**, *358*, 9–17. [CrossRef]
19. Ahmed, H.A.; Ismail, I.M.; Saleh, W.F.; Ahmed, M. Experimental investigation of humidification-dehumidification desalination system with corrugated packing in the humidifier. *Desalination* **2017**, *410*, 19–29. [CrossRef]
20. Ghaffour, N.; Bundschuh, J.; Mahmoudi, H.; Goosen, M.F. Renewable energy-driven desalination technologies: A comprehensive review on challenges and potential applications of integrated systems. *Desalination* **2015**, *356*, 94–114. [CrossRef]
21. Li, C.; Goswami, Y.; Stefanakos, E. Solar assisted sea water desalination: A review. *Renew. Sustain. Energy Rev.* **2013**, *19*, 136–163. [CrossRef]
22. Boyes, W. *Instrumentation Reference Book*, 3rd ed.; Elsevier Butterworth-Heinemann: Burlington, MA, USA, 2003; p. 272.
23. Kalogirou, S.A. *Solar Energy Engineering: Processes and Systems*, 2nd ed.; Academic Press: Waltham, MA, USA, 2013.
24. Rabl, A. *Active Solar Collectors and Their Applications*; Oxford University Press: New York, NY, USA, 1985.

25. Camacho, E.F.; Berenguel Soria, M.; Rubio, F.R.; Martínez, D. *Control of Solar Energy Systems*; Springer Science & Business Media: New York, NY, USA, 2012; pp. 25–47.
26. Wang, S.K. *Handbook of Air Conditioning and Refrigeration*, 2nd ed.; McGraw-Hill: New York, NY, USA, 2001.
27. Coccia, G.; Di Nicola, G.; Hidalgo, A. *Parabolic trough Collector Prototypes for Low-Temperature Process Heat*; Springer International Publishing AG Switzerland: Basel, Switzerland, 2016.
28. Goswami, D.Y.; Kreith, F.; Kreider, J.F. *Principles of Solar Engineering*, 2nd ed.; CRC Press (Taylor and Francis Group): Philadelphia, PA, USA, 2000.
29. Kreith, F.; Jan, F.K. *Principles of Solar Engineering*; Hemisphere Pub. Corp.: Washington, WN, USA, 1978.
30. Duffie, J.A.; Beckman, W.A. *Solar Engineering of Thermal Processes*; John Wiley & Sons: Hoboken, NJ, USA, 2013.
31. Abdel-Hady, F.; Shakil, S.; Hamed, M.; Alzahrani, A.; Mazher, A. Simulation and Manufacturing of an Integrated Composite Material Parabolic Trough Solar Collector. *Int. J. Eng. Technol.* **2016**, *8*, 2333–2345. [CrossRef]
32. Incropera, F.P.; Dewitt, D.P.; Bergman, T.L.; Lavine, A.S. *Fundamentals of Heat and Mass Transfer*, 6th ed.; John Wiley & Sons: Danvers, MA, USA, 2007.
33. Bejan, A.; Kraus, A.D. *Heat Transfer handbook*; John Wiley & Sons: Hoboken, NJ, USA, 2003; Volume 1.
34. Kröger, D.G. *Air-Cooled Heat Exchangers and Cooling Towers. Thermal-Flow Performance Evaluation and Design*; PennWell Corporation: Tulsa, OK, USA, 2004; Volume 1.
35. Jaber, H.; Webb, B.L. Design of Cooling Towers by the Effectiveness-*NTU* Method. *ASME J. Heat Transf.* **1989**, *111*, 837–843. [CrossRef]
36. Narayan, G.P.; Mistry, K.H.; Sharqawy, M.H.; Zubair, S.M.; Lienhard, J.H. Energy effectiveness of simultaneous heat and mass exchange devices. *Front. Heat Mass Transf.* **2010**, *1*, 023001. [CrossRef]
37. Kreith, F. *The CRC Handbook of Thermal Engineering*; CRC Press LLC: Boca Raton, FL, USA, 2000.
38. Çengel, Y.A.; Boles, M.A. *Thermodynamics: An Engineering Approach*, 5th ed.; McGraw-Hill: New York, NY, USA, 2006.
39. Sinnott, R.K. *Coulson & Richardson's Chemical Engineering, Chemical Engineering Design*, 4th ed.; Elsevier Butterworth-Heinemann: Oxford, UK, 2005; Volume 6.
40. Kabeel, A.E.; El-Said, E.M.S. Applicability of flashing desalination technique for small scale needs using a novel integrated system coupled with nanofluid-based solar collector. *Desalination* **2014**, *333*, 10–22. [CrossRef]
41. Towler, G.; Sinnott, R. *Chemical Engineering Design Principles, Practice and Economics of Plant and Process Design*; Elsevier Butterworth-Heinemann: Burlington, MA, USA, 2008.
42. El-Halwagi, M.M. Introduction to Sustainability, Sustainable Design, and Process Integration. In *Sustainable Design through Process Integration: Fundamentals and Applications to Industrial Pollution Prevention, Resource Conservation, and Profitability Enhancement*, 2nd ed.; IChemE, Elsevier: New York, NY, USA, 2017.
43. El-Dessouky, H.T.; Ettouney, H. *Fundamentals of Salt Water Desalination*; Elsevier Science B.V.: Amsterdam, The Netherlands, 2002.
44. Khisty, J.C.; Mohammadi, J.; Amekudzi, A.A. *Systems Engineering with Economics, Probability and Statistics*, 2nd ed.; J. Ross Publishing: Lauderdale, FL, USA, 2012.
45. Saudi Electricity Company Official Web Site. Available online: https://www.se.com.sa/en-us/Customers/Pages/TariffRates.aspx (accessed on 12 March 2018).
46. Sharshir, S.W.; Peng, G.; Yang, N.; Eltawil, M.A.; Ali, M.K.A.; Kabeel, A.E. A hybrid desalination system using humidification-dehumidification and solar stills integrated with evacuated solar water heater. *Energy Convers. Manag.* **2016**, *124*, 287–296. [CrossRef]
47. Zhani, K.; Bacha, H.B. Experimental investigation of a new solar desalination prototype using the humidification dehumidification principle. *Renew. Energy* **2010**, *35*, 2610–2617. [CrossRef]
48. Deniz, E.; Çınar, S. Energy, exergy, economic and environmental (4E) analysis of a solar desalination system with humidification-dehumidification. *Energy Convers. Manag.* **2016**, *126*, 12–19. [CrossRef]
49. Zubair, M.I.; Al-Sulaiman, F.A.; Antar, M.A.; Al-Dini, S.A.; Ibrahim, N.I. Performance and cost assessment of solar driven humidification dehumidification desalination system. *Energy Convers. Manag.* **2017**, *132*, 28–39. [CrossRef]
50. Behnam, P.; Shafii, M.B. Examination of a solar desalination system equipped with an air bubble column humidifier, evacuated tube collectors and thermosyphon heat pipes. *Desalination* **2016**, *397*, 30–37. [CrossRef]

51. El-Halwagi, M.M. A Shortcut Approach to the Design of Once-Through Multi-Stage Flash Desalination Systems. *Desalin. Water Treat.* **2017**, *62*, 43–56. [CrossRef]
52. Gabriel, K.J.; Noureldin, M.M.B.; Linke, P.; El-Halwagi, M.M. Optimization of Multi-Effect Distillation Process Using a Linear Enthalpy Model. *Desalination* **2015**, *365*, 261–276. [CrossRef]
53. Gabriel, K.; El-Halwagi, M.M.; Linke, P. Optimization Across Water-Energy Nexus for Integrating Heat, Power, and Water for Industrial Processes Coupled with Hybrid Thermal-Membrane Desalination. *Ind. Eng. Chem. Res.* **2016**, *55*, 3442–3466. [CrossRef]
54. Khor, C.S.; Foo, D.C.Y.; El-Halwagi, M.M.; Tan, R.R.; Shah, N. A Superstructure Optimization Approach for Membrane Separation-Based Water Regeneration Network Synthesis with Detailed Nonlinear Mechanistic Reverse Osmosis Model. *Ind. Eng. Chem. Res.* **2011**, *50*, 13444–13456. [CrossRef]
55. El-Halwagi, M.M. Synthesis of Optimal Reverse-Osmosis Networks for Waste Reduction. *AIChE J.* **1992**, *38*, 1185–1198. [CrossRef]
56. Al-Aboosi, F.Y.; El-Halwagi, M.M. An Integrated Approach to Water-Energy Nexus in Shale Gas Production. *Processes* **2018**, *6*, 52. [CrossRef]
57. Bamufleh, H.; Abdelhady, F.; Baaqeel, H.M.; El-Halwagi, M.M. Optimization of Multi-Effect Distillation with Brine Treatment via Membrane Distillation and Process Heat Integration. *Desalination* **2017**, *408*, 110–118. [CrossRef]
58. González-Bravo, R.; Ponce-Ortega, J.M.; El-Halwagi, M.M. Optimal Design of Water Desalination Systems Involving Waste Heat Recovery. *Ind. Eng. Chem. Res.* **2017**, *56*, 1834–1847. [CrossRef]
59. Baaqeel, H.; El-Halwagi, M.M. Optimal Multi-Scale Capacity Planning in Seawater Desalination Systems. *Processes* **2018**, *6*, 68. [CrossRef]
60. El-Halwagi, M.M. A Return on Investment Metric for Incorporating Sustainability in Process Integration and Improvement Projects. *Clean Technol. Environ. Policy* **2017**, *19*, 611–617. [CrossRef]
61. BIPM; IFCC; IUPAC; ISO. *Evaluation of Measurement Data Guide for the Expression of Uncertainty in Measurement*; JCGM 100: Sèvres Cedex, France, 2008.